Computers and Fluids 269 (2024) 106123

Contents lists available at ScienceDirect

Computers and Fluids

journal homepage: www.elsevier.com/locate/compfluid

# Stability analysis of a streaky boundary layer generated by miniature vortex generators

András Szabó [a,*], Péter Tamás Nagy [a], Gilles De Baets [b], Maarten Vanierschot [b,c], György Paál [a]

[a] Department of Hydrodynamic Systems, Faculty of Mechanical Engineering, Budapest University of Technology and Economics, Bertalan Lajos u. 4 - 6, Budapest, H-1111, Hungary

[b] Department of Mechanical Engineering, KU Leuven, Leuven, Belgium

[c] Material Science, Innovation and Modelling (MaSIM), North-West University, Mmabatho 2745, South Africa

ARTICLE INFO

*Keywords:*
Boundary layer
Flow stability
Transition delay
Miniature vortex generator

ABSTRACT

Delaying laminar-turbulent transition is an attractive method to reduce friction drag on streamlined bodies. In the case of natural transition, in which turbulence is triggered by the growth of two-dimensional Tollmien–Schlichting (TS) instabilities, this growth of TS instabilities can be attenuated by introducing steady streamwise streaks into the boundary layer. These streamwise streaks are generated by streamwise vortices, which rearrange the flow via the lift-up mechanism. Such streamwise vortices can be induced by so-called miniature vortex generators (MVGs). Although recently considerable attention has been devoted to the investigation of MVGs, and multiple studies investigated MVGs with different parameters, the previously investigated MVG configurations are likely suboptimal. This study aims at (partially) filling this knowledge gap by complementing previous studies by conducting a parametric study of rectangular MVGs and assessing them with local linear stability analysis. Three parameters are varied simultaneously: the height, the spanwise distance of the MVG pairs, and the distance between MVGs in each pair. First, the modelling approach is presented, which consist of an efficient base flow computation, and BiGlobal stability analysis. The base flow calculation is validated by comparing our results with the experiments of Shattarzadeh and Fransson (2015). Then, the streak amplitude, the growth factors of the TS-waves and the secondary shear-layer instabilities are analysed in a parametric study. It is shown that with the variation of the spanwise distances, the maximum amplitude and the streamwise extent of the streaks in the boundary layer can be controlled, reminiscent of the behaviour of the optimal vortices. The findings and the test of the methodology provide valuable insight, which may be useful for the optimisation of MVGs.

## 1. Introduction

Delaying laminar-turbulent transition over streamlined aerodynamic bodies has been an actively researched field for a long time, as it is a very promising technique to reduce the drag of streamlined bodies. There are two main categories of the transition scenario: transition due to boundary layer instability and bypass transition [1]. The former scenario is the dominant one in a low free-stream turbulence environment, while the latter prevails when the free-stream turbulence level is high. Bypass transition, although it has been a subject of a large body of research, is not understood well, and this transition scenario, due to its stochastic nature and several possible routes, is a less suitable target for flow control. Transition through the development of instability waves is much more suitable for flow control, as it is both better understood and more relevant in cruise conditions. In this transition scenario, the exponential amplification of small-amplitude disturbances is dominant, which can be appropriately described by linear stability theory. After the disturbance amplitude reaches a certain threshold, nonlinear effects set in; this is the secondary instability phase, which covers a much smaller spatial extension of the linear instability [2]. Several instability mechanisms exist; in the case of an incompressible two-dimensional boundary layer with small-to-none surface curvature, the dominant instability mechanism is the two-dimensional Tollmien–Schlichting (TS) wave. This is a well-understood, classical instability mechanism, and the dampening of the TS waves is the main interest of our research.

Several control techniques exist to modify the flow so that the transition is shifted downstream, e.g., wall-movement, surface heating, suction, shape optimisation [3] or localised surface modification [4]. Special structures, such as riblets, have also been applied to transition-delay: they delay the growth of Görtler-type instabilities but they do

* Corresponding author.
*E-mail address:* aszabo@hds.bme.hu (A. Szabó).

https://doi.org/10.1016/j.compfluid.2023.106123
Received 24 April 2023; Received in revised form 30 August 2023; Accepted 13 November 2023
Available online 17 November 2023

not damp the growth of TS waves [5]. Another promising method to attenuate TS waves is the introduction of periodically varying slow–fast regions, so-called streamwise streaks into the boundary layer. It was shown both in numerical [6] and laboratory experiments [7] that with properly generated streaks, TS waves can be dampened. The physical mechanism of the TS wave attenuation is also clear: the spanwise shear generated by the streaks in the boundary layer is responsible for decreasing the disturbance energy growth [6]. Control strategies relying on the generation of spanwise shear are called as *methods of spanwise mean velocity gradients* (SVG) [8].

Although SVG can also be generated by spanwise elongated roughness elements [9], creating boundary layer streaks is the most promising technique for stabilisation. Streaks in a boundary layer can be generated in several ways [10]. Generally, the higher the streak amplitude, the stronger this stabilisation [6]. However, a too high streak amplitude is not desirable since then streaks themselves become unstable to inviscid secondary sinuous instabilities[1] [11], which can result in an early breakdown to turbulence; a well-known mechanism that also plays a role as free-stream turbulence enters the boundary layer [12]. Therefore, the generation of appropriate streaks is a problematic topic. Although streaks introduced with discrete suction [13] and pairs of oblique waves [14] were proven to be able to delay transition, passive surface elements are more desirable since they do not require an external energy source. Earlier studies used cylindrical roughness elements [7] for this purpose. Unfortunately, such roughness elements were only capable of generating streaks with moderate strength, since increasing the roughness height would destabilise the wake of the roughness elements.

A promising passive technique was reported by Shahinfar et al. [15]: using winglet-type miniature vortex generators (MVGs), strong streaks can be generated; therefore, effective stabilisation of the boundary layer can be achieved, while the streaks remain stable. Following experimental studies [16–20] report additional information regarding the MVGs, such as: how changing a single parameter of the MVGs independently affect the boundary layer; how using a second MVG row can reinforce the streaks that decay downstream; the instability growth in the near-field of the MVGs, and also further downstream; the effect of the pressure gradient. Furthermore, the stabilisation of the TS waves [19] and oblique disturbances [21] were also observed experimentally in a streaky boundary layer introduced by MVGs. In most of these studies, triangular MVGs were used, except for the investigations of Sattarzadeh and Fransson [19,22], who examined rectangular MVGs. The above mentioned experimental studies firmly established that MVGs are able to successfully generate a streaky boundary layer in which the growth of the TS waves is attenuated. Motivated by the above findings recently, Weingärtner et al. [23] set out to conduct wind tunnel measurements targeted at application of the MVGs on the fuselage of the laminar aircraft Otto Celera 500L of Otto Aviation company. They have developed a design procedure that can provide recommendations for the parameters of the MVGs.

The numerical flow stability investigation of streaky boundary layers has also received some attention. Most of the numerical studies focused on boundary layers stabilised by idealised vortices. Bagheri and Hanifi [24] used nonlinear Parabolised Stability Equations (PSE) to investigate the optimal spacing of the streaks in the Blasius boundary layer to suppress TS waves. However, although they have shown that with a sufficient spanwise spacing, a weaker flow modification can also enhance the stability of the flow, their study is incomplete. They only examined high frequency instabilities, and therefore a short streamwise region. TS waves trigger transition considerably more downstream in a low external disturbance environment, which is not covered in their study. Siconolfi et al. [25] also examined the Blasius boundary layer perturbed by streamwise vortices. They used direct numerical simulation (DNS) of the Navier–Stokes (NS) equations for the base flow calculation, and BiGlobal stability analysis to model the instability waves. They showed that placing the vortices at the edge of the boundary layer can be much more effective for streak generation than vortices inside the boundary layer. The reason for this is that streamwise vortices generate streaks through the lift-up mechanism [26]: they move fast fluid from the free stream to the boundary layer and vice versa. Vortices placed too much inside or outside the boundary layer utilise the lift-up mechanism suboptimally: the optimal wall-normal placement of the vortices ensures the persistence of the streaks. Martín and Paredes [27] used slightly different numerical techniques to investigate the same phenomena as Siconolfi et al. [25]. They calculated the evolution of streaks with Boundary Region Equations (BRE), and the evolution of the disturbances is calculated with linear PSE. The BRE are much more effective than DNS, if the slowly varying assumption holds; moreover, PSE is a sophisticated tool that includes both non-local and non-parallel effects in slowly varying flows. They validated the use of BRE for streak amplitude calculation by finding essentially the same streak amplitudes as Siconolfi et al. [25]. Their neutral curves of secondary instabilities calculated with PSE were different (by roughly 5%) from those calculated with BiGlobal stability equations, because of non-local effects. More recently, Martín and Paredes [28] examined streaks with limited maximum amplitude that were generated using optimal disturbances. Their main finding is the extension of the results of Bagheri and Hanifi [24]: the spanwise wavenumber and the maximum amplitude of the boundary layer streaks both have a significant influence not only on the attenuation of the TS waves but also on the sinuous secondary instabilities. Furthermore, they predicted the transition location using the $e^N$ method.

The numerical calculations using idealised vortices provide valuable insight to the stability of the streaky boundary layer. Nevertheless, the practical realisation of idealised vortices is a challenging task yet to be investigated. Due to the cumbersomeness of experiments, numerical calculation offers an alternative to study a large number of flow configurations. However, only two studies were dedicated to the numerical investigation of the flow stability in a realistic MVG configuration. The first one was performed by Siconolfi et al. [29], who used direct numerical simulation to calculate the base flow and BiGlobal stability analysis to calculate the instability of the flow. They reproduced two experimental configurations of their results with the experiments of Shahinfar et al. [17], and compared their results with the measurements finding reasonable agreement. They identified several unstable modes in the downstream vicinity of the MVGs, which cause local disturbance growth that might result in a premature transition to turbulence. They noted that since the MVG scatters instabilities into multiple modes that cannot be distinguished in experiments, comparing the numerical and experimental disturbance growth is problematic relatively close to the MVGs. The second study was recently presented by Nobis et al. [30]. They performed topological optimisation of MVGs using the temporal formulation of direct-adjoint looping of the linearised Navier–Stokes equations, aiming at minimising the energy of the TS waves that impinge on the MVGs at a downstream location. They managed to improve their MVGs substantially; however, they did not consider the spanwise spacing of the vortex generators as an optimisation parameter, which has a strong effect on the streak evolution as Sattarzadeh and Fransson [22], Bagheri and Hanifi [24] and Martín and Paredes [28] demonstrated. For more details on the optimisation procedure of Nobis et al. [30], the interested reader is referred to their previous study on superhydrophobic surfaces [31].

The above studies all involved low-speed flat plate boundary layers, where the compressibility and curvature effects can be neglected. However, for the sake of completeness, we note that in high speed

[1] The term *secondary instability* refers to the fact that the secondary instability mechanism exists in the flow that consists of the equilibrium boundary layer plus a primary instability mechanism. The primary instability can be a finite amplitude TS wave [2], or a streamwise vortex that generates streaks through the lift-up instability [11].

flows transition delay using techniques similar to MVGs have also received considerable attention. In the case of swept wings, the dominant instability mechanism is the stationary crossflow instability. These instabilities were found to be attenuated by discrete roughness elements (DRE) [32]. Despite the signifiant attention this flow control mechanism has received, recent flight tests [33] show that the underlying phenomena are still not properly understood. In the case of hypersonic flows, it was found that Mack-mode (or second mode) instabilities can be delayed with streaks generated by artificial vortices on cones [34] and flat plates [35]. These studies were followed by simulations utilising vortex generators for the same purpose [36]. Then, shape optimisation of the vortex generators was performed [37,38] to increase the efficiency of their previous baseline configuration. However, similarly to Nobis et al. [30], they did not consider the spanwise spacing of the MVG, which is known to have a significant effect on the stability of the flow.

The paramount importance of accurate modelling of transition delay techniques is well illustrated in [33]; therefore, their main findings are outlined briefly. As mentioned previously, Saric et al. [33] was concerned with the disruption stationary crossflow vortices, using DREs. This flow control method relies on using roughness elements whose spanwise periodicity is smaller than that of the dominant crossflow instability. Despite the success of initial experiments in low turbulence level wind tunnels, in-flight tests of the DRE with the SWIFT swept wing model could only observe transition delay in 6 out of 112 cases. This motivated the researchers to upgrade the measurement configuration w.r.t the uncertainties, measurement techniques, surface roughness, etc., [33] reports the results of the improved SWIFTER experimental configurations. Despite the precise work of the experimentalist, only a single test out of 30 showed transition delay; furthermore, although six attempts were made to reproduce the transition delay, none of them were successful. The experimentalists conclude their paper by stating that "The main recommendation of this research effort is to further investigate DREs computationally". These results regarding the DRE highlight the important role of computational modelling of MVGs to make the technology suitable for commercial applications. Therefore, although quantitative recommendations for real-world use of MVGs, such as those given by Weingärtner et al. [23] are extremely valuable, they should be utilised for engineering applications with caution.

Based on the large body of literature concerned with the stabilisation of the TS waves by streamwise streaks, and more specifically, streaks induced by MVGs, several open questions can be identified. Addressing any of the topics listed below may improve the Technology Readiness Level of the flow control strategy:

(i) Studies in which the MVGs are substituted with idealised vortices suggest that the previously proposed triangular and rectangular MVG geometries are not ideal. Fransson and Talamelli [16] were the first to investigate MVGs for TS wave attenuation, and their MVGs serve as the base configuration for subsequent studies. They note regarding the triangular MVG configuration which they proposed that "The present design follows the criterion suggested by Pearce (1961) for persistent streamwise existence of the vortices". However, Pearce [10] reports experiments in which vortex generators were investigated in connection with shock-induced separation. The report of Gould [39] also mentions vortex generators with a height larger than the boundary layer thickness (see figures 2c and 26 in his work). This means that the recommendations of Pearce [10] are formulated for significantly higher MVGs than those investigated by Fransson and colleagues. Therefore, their vortex generator parameters are probably not ideal for transition delay in incompressible boundary layers. As such, the investigation of new, better MVG geometries is also an open topic.

(ii) In experimental studies, due to their cumbersomeness, only a limited number of configurations were tested: each time only a single parameter was varied with respect to a basic configuration. Although functional relationships were obtained between the MVG parameters and the amplitude of the streaks, the range of validity of such relations is likely to be limited. Numerical methods allow to cover a much larger parameter space more efficiently. However, until now numerical studies have only considered idealised vortices, whose relationship to real MVG geometries is unknown. Therefore, computational investigation of the relationship between the MVG parameters and the stability of the streaky boundary layer is necessary.

(iii) The influence of pressure gradient, curvature and compressibility effects should be examined for aerospace applications.

(iv) So far, mostly the stability of a streaky boundary layer generated by the MVGs was studied computationally. However, the stability of the near-MVG flow field should also be investigated. This should cover absolute (wake-type) instability, scattering of instabilities impinging on the MVGs and scattering of large wavelength free-stream fluctuations and acoustic waves into instabilities [40].

(v) Not only the linear, but also the nonlinear evolution of the instabilities should be considered.

(vi) The robustness of the flow control strategy w.r.t manufacturing imperfections, freestream velocity variation, and crossflow should also be investigated.

### 1.1. Optimisation of the MVGs

The study is concerned with partially addressing the first two points: working towards the computational optimisation of MVGs using linear stability analysis. Before stating the goals, however, all transition scenarios that together define the absolutely optimal MVG, along with the state-of-the-art modelling tools, are reviewed. Although in the review of the transition process some of the previous points are repeated, the discussion helps clarify the scope of the present study, with both the strengths and weaknesses of the modelling procedure.

First, the stability of the flow field around the MVGs, and its downstream vicinity has to be considered, which we refer to as objective 1 (Obj. 1). Here, two physical mechanisms are important. On the one hand, the stability of the TS waves impinging on the MVGs need to be assessed. On the other hand, the MVG as a receptivity agent must also be considered. MVGs, as local boundary layer modulations, can scatter large length-scale free-stream fluctuations (e.g., vorticity (gusts) and acoustic waves) into shorter length-scale instabilities through the long–short wave conversion mechanism [41]. Since the flow around the MVG is fully three-dimensional, classical local stability methods cannot be used. The solution of the global stability problem in the temporal domain is a possibility; however, input–output formalism in the frequency domain, which is a special case of the global resolvent analysis [42] is likely to be better suited for the analysis of the MVGs.

In global input–output framework, the TS waves can be considered as a boundary condition at the upstream end of the domain (input), and the downstream end of the computational domain is the output. The receptivity problem is more problematic. It is customary to solve for the 'worst-case' disturbances that yield the highest kinetic energy amplification called optimal disturbances; in essence, these are the leading input and output modes of the singular value decomposition of the resolvent operator [42]. However, these optimal disturbances are not necessarily meaningful as they are not likely to manifest themselves in practice. The recently proposed method of Kamal et al. [43], which restricts the input of the resolvent operator to forcing induced by plane-wave solutions outside the boundary layer, could be used to provide accurate receptivity predictions.

Solving the resolvent-problem in a fully three-dimensional setting requires large computational resources; even with recent advancement

in iterative methods [44], a supercomputer is required to solve the problem. This can be partially remedied by using the global resolvent to calculate the response of the flow around the MVG, and the recently proposed one-way Navier Stokes (OWNS) [45,46] formalism in the close downstream vicinity of the MVGs. The OWNS, unlike the PSE formalism, are well-posed set of boundary layer-like equations that can be marched downstream to obtain the solution, while it also allows one to capture non-modal effects, which are not included in PSE. The combination of the two techniques could be used to optimise the MVGs to suppress the disturbance growth relatively near them, using either a direct-adjoint formalism [47], Bayesian optimisation [48], or possibly, automatic differentiation [49,50]. We note that three-dimensional resolvent-based optimisation is computationally challenging [51]; the authors are only aware of using it as a tool to provide recommendation for design [52].

We note that nonlinear extension of both the global input–output formalism [53] and the OWNS approach [54] is also possible, which may be important to capture nonlinear interaction. The zero frequency nonlinear interaction, called mean flow distortion (MFD), which is the difference between the mean flow and the base flow, can be especially important: MFD, by its nature, can cumulate large values over extended spatial intervals, exert a large effect on the stability of the flow. However, the computational cost of the nonlinear methods is even higher than that of their linear counterpart.

An MVG that satisfies Obj.1 suppresses disturbance growth in its proximity, and disturbances decay in its downstream vicinity. Then, after some distance downstream, the boundary layer becomes convectively unstable once again as the streaky structures become weaker. Therefore, the growth of the TS waves is expected to drive the laminar-turbulent transition. The second objective (Obj. 2) of flow control with MVGs is that they delay the growth of TS waves far downstream.

The stability of the TS waves in a streaky boundary layer is well-described by modal stability analysis. BiGlobal stability equations [55], a local stability equation may be used to describe the TS waves. As an alternative to BiGlobal stability equations, plane-marching PSE [56, 57] can be utilised, which includes non-local effects that can have a substantial effect on the stability of the flow. Finally, the recently developed adaptive harmonic linearised Navier–Stokes [58] formalism could be extended to fully-three-dimensional flow, which offers a more sophisticated alternative to PSE that does not contain the ill-posedness stemming from the ad-hoc parabolisation. Using the growth rates from the modal stability calculations, the transition location can be estimated using the $e^N$ method [59] in a two-dimensional boundary layer. The $e^N$ method relies on the observation that transition to turbulence correlates strongly with the growth of the instability waves in a low disturbance environment. It is reasonable to assume that the $e^N$ method can be used in a streaky boundary layer to predict transition initiated by the three-dimensional TS waves, despite the fact that it ignores many of the previously mentioned physical phenomena.

The optimisation of the MVGs w.r.t the above two objectives (the stability of the flow around the MVG, and the stability of the TS waves in the streaky boundary layer) has two constraints. First, the flow around the MVG should not be absolutely unstable, as bluff-body-like vortex-shedding is expected to advance transition. The absolute instability can be detected either with local absolute [60] or global stability analysis of the three-dimensional base flow or by temporal DNS of the linear or nonlinear NS equations. Second, the streaks should not exhibit the secondary sinuous instability that can also cause premature transition [12,26]. The secondary sinuous instability is a well-understood modal mechanism [11,27] that can be well described with the same tools as TS waves.

As outlined, the global optimisation of MVGs w.r.t. all objectives and constraints is a tremendous task. The previous studies optimising MVGs only considered partial objectives. Pederson et al. [37] and Klauss et al. [38] optimised the shape of the MVGs w.r.t. the streamwise integral of the streak amplitude, which corresponds to *indirectly* optimising for Obj. 2, as the streak amplitude correlates with the attenuation of the primary instability (in their case the Mack-modes). Their constraint was a limit on the maximum value of the streak amplitude, which correlates with the secondary instability. Therefore, these authors did not consider the stability of the flow field near the MVGs. The study of Nobis et al. [30] performed shape optimisation with direct-adjoint looping, and solved the global stability equations in a temporal framework. Their optimisation objective was minimising the disturbance amplitude relatively close downstream of the MVGs, which can be considered as an optimisation for Obj. 1, although they did not consider the receptivity process.

### 1.2. Objectives of the study

In this study, the stability of the streaky boundary layer generated by MVGs mounted on a zero pressure gradient flat plate is characterised using local modal linear stability analysis. Considering the optimality of the MVGs, the objectives are the same as in [37,38]: Obj. 2. - attenuation of the primary instabilities, while avoiding the emergence of secondary instability modes. It is stressed that the present study focuses only Obj. 2 of the multi-objective optimisation. Therefore, since Obj. 1 is not considered, it is not clear that the present recommendations yield improved MVGs in all aspects. Instead of using the streak amplitude as an indirect measure of the stabilisation/destabilisation of the boundary layer like [37,38], local stability equations are solved to characterise the flow using the $e^N$ method. Two $N$ factors are calculated: one for the TS waves, and one for the secondary instabilities. Although using two $N$ factors to characterise the stability of the flow may be unusual, it is not a new concept: Schrauf [61] successfully used two $N$ factors – one for the stationary crossflow instability, and one for the TS waves – to successfully correlate local stability calculations with in-flight test data.

The $e^N$ method utilised in our study may seem primitive compared to the recently developed analysis tools. However, the fact that the $e^N$ method is still extensively used in industrial studies [62,63], can be attributed to the following: it is simple, it has a relatively low computational cost, yet it captures a substantial amount of the underlying physics of the transition process. The 'success' of the $e^N$ method suggests that it can provide predictions, recommendations in the development of MVGs. These recommendations can reduce the total number of parameters, after which optimisation can be performed for Obj. 1, which is a much more computationally demanding task because of the fully three-dimensional nature of the problem.

The choice of local modal stability analysis instead of non-local equations, i.e., BiGlobal stability instead of PSE, is also motivated by the goal of reducing the large parameter space of all possible MVG configurations. BiGlobal stability equations can be much more easily setup and automated than PSE, since PSE requires the specification of the local stability solution as an initial condition. At this level of modelling, it is beneficial to trade accuracy for a more automated work flow; these choices are highlighted in the discussion of the methodology and the results. After the identification of the favourable parameter region, more sophisticated tools can be used for more accurate modelling. To illustrated this, at the end of our study, BiGlobal stability equations are compared with plane-marching PSE.

In the present study, rectangular MVGs are modelled, and their parameters are varied. The simple geometry allows the variation of parameters such as the spanwise distance, which a were not considered in previous studies performing topological optimisation [30,37,38]. Therefore, our complementary approach can help to improve the optimisation of different geometries. With the parametric study, the goal is to learn more about the flow field, and set up a reliable framework for future optimisation of the streaky structures.

The calculation of the stationary laminar base flow is carried out in an efficient manner: the near-field of the MVG is calculated using commercial 3D CFD software, and the downstream evolution of the streaky

**Table 1**
Parameters of the base MVG and the computational setup.

| $\hat{\Lambda}$ (mm) | $\hat{d}$ (mm) | $\hat{h}$ (mm) | $\hat{w}$ (mm) | $\hat{L}$ (mm) | $\Theta$ (°) | $\hat{x}_{\mathrm{MVG}}$ (mm) | $\hat{x}_0$ (mm) | $\hat{x}_{\mathrm{st}}$ (mm) | $\hat{x}_{1,\mathrm{CFD}}$ (mm) |
|---|---|---|---|---|---|---|---|---|---|
| 13 ($3.60\hat{\delta}_{99,\mathrm{MVG}}$) | 3.25 ($0.90\hat{\delta}_{99,\mathrm{MVG}}$) | 1.3 ($0.36\hat{\delta}_{99,\mathrm{MVG}}$) | 0.3 ($0.08\hat{\delta}_{99,\mathrm{MVG}}$) | 3.25 ($0.90\hat{\delta}_{99,\mathrm{MVG}}$) | 9 | 222 | 213 | 235 | 240 |

boundary layer was calculated by solving the BRE. In the calculation of the base flow, essentially the methodology of Siconolfi et al. [29] and Martín and Paredes [27] is combined. Both the BRE and BiGlobal stability equations are solved using an in-house code, written in the parallel version of the open-source finite element language FreeFem [64] in combination with the open-source computational toolkits PETSc [65,66] and SLEPc [67]. The previously discussed aspects – the configuration, modelling, and the numerical techniques – can be found in Sections 2.1–2.3, respectively.

After discussion of the methodology and numerical techniques, first, the experiments of Sattarzadeh and Fransson [22] are modelled, which is covered in Section 3.1. These authors performed measurements of the flow-field, modified by the MVGs, in a low turbulence intensity wind-tunnel using hot-wire probes. They varied three parameters of the configuration, one at a time: the angle, the spanwise periodicity, and the free-stream velocity. The authors present results on the streak amplitude, as a measure of the boundary layer modulation. Furthermore, low amplitude TS waves were excited upstream of the MVGs using slots, in which alternating blowing-suction was induced by loudspeakers. The amplitude of the TS waves, measured by the integral of the streamwise velocity fluctuation in a plane, is also given by the experimentalists. The streak amplitude from the base flow calculation is compared with the experimental data in detail to validate the methodology. Meaningful comparison of the stability calculation is, because of ou modelling approach, limited.

After a comparison with the experiments, three parameters of the MVG — the spanwise periodicity, the distance between the individual MVG pairs, and the MVG height are varied simultaneously in a parametric study. The effect of varying the MVG parameters is discussed in detail for both the streaky base flow (Section 3.2) and its stability (Section 3.3). Finally, additional aspects as roughness-induced transition, absolute instability, and comparison of the BiGlobal and plane-marching PSE calculations are briefly discussed in Section 3.4. Conclusions are drawn in Section 4.

## 2. Flow configuration and modelling

### 2.1. Flow configuration

A zero pressure gradient incompressible boundary layer is considered. $x$, $y$ and $z$ denote the streamwise, wall-normal and spanwise coordinates, respectively. Dimensional quantities are denoted with a hat ($\hat{\square}$), while nondimensional quantities are denoted with regular letters. The configuration is the same as studied by Sattarzadeh and Fransson [22], and their C02 case is taken as the basis of the present study; with respect to this case, the height, the inner distance and the spanwise periodicity are varied in the parametric study. Therefore, the free-stream velocity and kinematic viscosity are $\hat{U}_\infty = 6$ m/s and $\hat{\nu} = 1.4607 \cdot 10^{-5}$ m$^2$/s, respectively. The problem setup is displayed in Fig. 1. $\hat{x}_{\mathrm{MVG}}$ denotes the downstream distance of the MVG centre from the start of the idealised leading edge. The spanwise distance between two MVGs in denoted with $\hat{d}$, while, the spanwise distance between MVG pairs is $\hat{\Lambda}$. The width, length and height of the MVGs are $\hat{w}$, $\hat{L}$ and $\hat{h}$, respectively. Finally, the angle of the MVG with the free-stream velocity is $\hat{\theta}$. The values of the parameters can be found in Table 1; as a reference, their ratio to the boundary layer thickness at the MVG ($\hat{\delta}_{99,\mathrm{MVG}} = 3.610$ mm) is also displayed.

### 2.2. Modelling

The incompressible flat plate boundary layer is investigated using linear stability analysis. The total velocity field is decomposed into a stationary equilibrium solution, called base-flow, and a small amplitude perturbation around the base flow. Let $\mathbf{U} = [U, V, W]^T$ and $P$ denote the base flow velocity and pressure, and $\mathbf{u}' = [u', v', w']^T$ and $p'$ the velocity and pressure of the small-amplitude perturbations. Then, the governing equations of the base flow are

$$(\mathbf{U} \cdot \nabla)\mathbf{U} = -\nabla P + \frac{1}{\mathrm{Re}}\nabla^2 \mathbf{U}, \tag{1}$$

$$\nabla \cdot \mathbf{U} = 0. \tag{2}$$

Eqs. (1)–(2) are nondimensionalised with the free-stream velocity $\hat{U}_0$ and boundary layer length scale $\hat{\delta}_0 = \sqrt{\hat{L}_0 \hat{\nu}/\hat{U}_\infty}$. $\hat{L}_0 = \hat{x}_{st}$ (defined in Section 2.3; see also Fig. 1(a)), and $\mathrm{Re} = \hat{\delta}_0 \hat{U}_\infty/\hat{\nu}$ is the Reynolds number. The nondimensional pressure is $P = \hat{P}/(\hat{\rho}\hat{U}_\infty^2)$.

Eqs. (1)–(2) are used to describe the base flow in the near field of the MVG (brown box in Fig. 1(a)), where the variation of the flow field is large in all three directions. However, after some distance downstream of the MVG, Eqs. (1)–(2) can be considerably simplified, while retaining the accuracy, using some scaling assumptions. It is reasonable to consider that the variation of the flow field is small in the streamwise, and large in the wall-normal and spanwise directions. Furthermore, the spanwise and wall-normal velocities can be assumed to be smaller than the streamwise velocity. Therefore, Eqs. (1)–(2) can be simplified by using a different nondimensionalisation for the different variables. Introducing the small parameter $\varepsilon = 1/\sqrt{\hat{L}_0 \hat{U}_\infty/\hat{\nu}}$, scaled coordinates $[\tilde{X}, \tilde{Y}, \tilde{Z}]^T = [\hat{x}/\hat{L}_0, \hat{y}/(\varepsilon \hat{L}_0), \hat{z}/(\varepsilon \hat{L}_0)]^T$, scaled velocities $[\tilde{U}, \tilde{V}, \tilde{W}]^T = [\hat{U}/\hat{U}_\infty, \hat{V}/(\varepsilon \hat{U}_\infty), \hat{W}/(\varepsilon \hat{U}_\infty)]^T$ and scaled pressure $\tilde{P} = \hat{P}/(\varepsilon^2 \hat{\rho} \hat{U}_\infty^2)$, we get

$$\begin{aligned}
\tilde{U}\frac{\partial \tilde{U}}{\partial \tilde{X}} + \tilde{V}\frac{\partial \tilde{U}}{\partial \tilde{Y}} + \tilde{W}\frac{\partial \tilde{U}}{\partial \tilde{Z}} &= \frac{\partial^2 \tilde{U}}{\partial \tilde{Y}^2} + \frac{\partial^2 \tilde{U}}{\partial \tilde{Z}^2}, \\
\tilde{U}\frac{\partial \tilde{V}}{\partial \tilde{X}} + \tilde{V}\frac{\partial \tilde{V}}{\partial \tilde{Y}} + \tilde{W}\frac{\partial \tilde{V}}{\partial \tilde{Z}} &= -\frac{\partial \tilde{P}}{\partial \tilde{Y}} + \frac{\partial^2 \tilde{V}}{\partial \tilde{Y}^2} + \frac{\partial^2 \tilde{V}}{\partial \tilde{Z}^2}, \\
\tilde{U}\frac{\partial \tilde{W}}{\partial \tilde{X}} + \tilde{V}\frac{\partial \tilde{W}}{\partial \tilde{Y}} + \tilde{W}\frac{\partial \tilde{W}}{\partial \tilde{Z}} &= -\frac{\partial \tilde{P}}{\partial \tilde{Z}} + \frac{\partial^2 \tilde{W}}{\partial \tilde{Y}^2} + \frac{\partial^2 \tilde{W}}{\partial \tilde{Z}^2},
\end{aligned} \tag{3}$$

$$\frac{\partial \tilde{U}}{\partial \tilde{X}} + \frac{\partial \tilde{V}}{\partial \tilde{Y}} + \frac{\partial \tilde{W}}{\partial \tilde{Z}} = 0. \tag{4}$$

Eqs. (3)–(4) are called boundary region equations (BRE). This is a well known extension of the boundary layer equations. The BRE were previously used for several different flow problems, and their use to model the evolution of streamwise streaks was validated [27,68]. These equations are parabolic, and with suitable initial- and boundary conditions well-posed. Thus, they can be marched downstream using a reasonable step size without any further restriction. The BRE are used to calculate the base flow downstream of the MVG, in the region displayed by the blue box. Note that the flow quantities calculated with the solution of the BRE were rescaled to the regular nondimensionalisation with $\hat{\delta}_0$ for the stability calculations.

The modulation of the base flow, i.e., the strength of the streaks is measured by the streak amplitude. Two definitions were proposed [17]: the integral and difference-based streak amplitudes, which are the following:

$$A_{\mathrm{ST}}^{\mathrm{int}}(x) = \int_{-0.5}^{0.5}\int_{0}^{\eta_1} |U(x,\eta,\zeta) - U^{\zeta}(x,\eta)| \mathrm{d}\eta \mathrm{d}\zeta, \tag{5}$$

$$A_{\mathrm{ST}}^{\mathrm{diff}}(x) = \frac{1}{2}\max_y \left[\max_z \{U(x,y,z)\} - \min_z \{U(x,y,z)\}\right]. \tag{6}$$

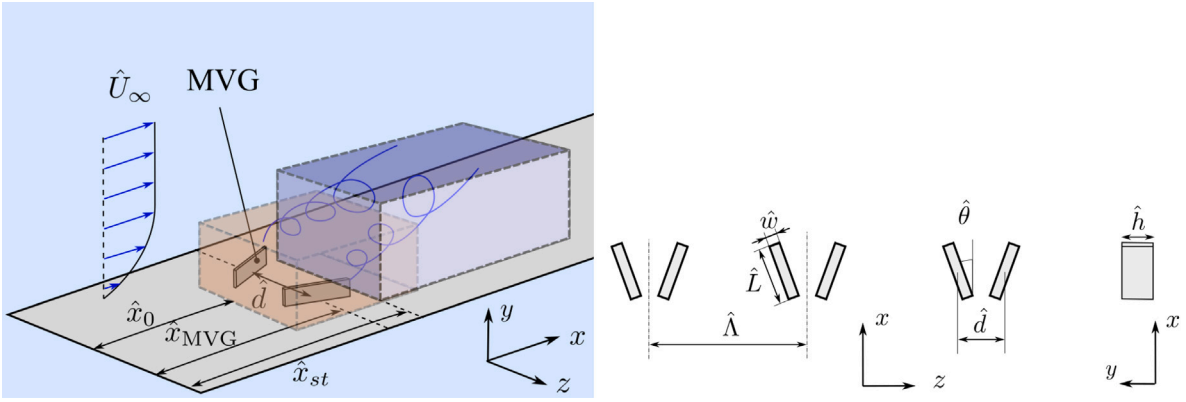


(a) Flow configuration (b) Geometric parameters of the MVG

**Fig. 1.** Flow configuration and parameters.

In the equation above, $\eta = \hat{y}/\hat{\delta}(x)$ is the wall-normal coordinate scaled with the *local* boundary layer scale, and $\eta_1$ is a sufficiently high wall-normal location where the boundary layer modulation vanishes, $\zeta = \hat{z}/\hat{\Lambda}$, and $U^\zeta$ is the spanwise averaged velocity. The integral-based definition is argued to be a better measure of the stabilisation, since it also accounts for the spanwise extent of the spanwise shear that stabilises the TS waves [17]. The difference-based amplitude is more suitable to measure the destabilisation, since above a critical value of 0.26, secondary instabilities arise in the case of optimal streaks [11].

Finally, in the linear stability framework, the linearised Navier–Stokes equations that describe the perturbations are

$$\frac{\partial \mathbf{u}'}{\partial t} + (\mathbf{U}\cdot\nabla)\mathbf{u}' + (\mathbf{u}'\cdot\nabla)\mathbf{U} = -\nabla p' + \frac{1}{\mathrm{Re}}\nabla^2\mathbf{u}', \tag{7}$$

$$\nabla\cdot\mathbf{u}' = 0. \tag{8}$$

Since the stability of the streaky boundary layer is investigated (the stability analysis of the near field of the MVGs is beyond the scope of this study), due to the small base flow variation in the streamwise direction, it is reasonable to seek disturbances in the form

$$\mathbf{q}'(x,y,z,t) = \mathbf{q}(y,z)e^{\mathrm{i}(\alpha x-\omega t)} + \text{c.c.}, \tag{9}$$

where $\mathbf{q} = [u, v, w, p]$. In the equations above, $\alpha$ is the streamwise wavenumber, $\omega$ is the angular frequency, i is the imaginary unit and c.c. stands for complex conjugate. In the case of a spatial stability analysis which is more appropriate for boundary layers, $\omega$ is real and is the prescribed input, while the complex wavenumber $\alpha$ is the eigenvalue sought. Substituting the above ansatz into Eqs. (7)–(8), the following problem can be derived:

$$(\alpha^2\mathbf{A}_2 + \alpha\mathbf{A}_1 + \mathbf{A}_0)\mathbf{q} = 0. \tag{10}$$

The above equations are called BiGlobal stability equations [55], and have been widely applied to study various flows. The coefficient matrices in the above problem can be found in [69]. In the BiGlobal stability equations, the spatial growth rate $\mu$ can be calculated as the imaginary part of the complex wavenumber $\alpha$: $\mu = \alpha_i$. Eq. (10) is a polynomial eigenvalue problem, which can be transformed into a generalised eigenvalue problem via the companion matrix method [70], for which standard solution techniques are available.

The discussion is continued with the plane-marching PSE methodology. As an alternative to Eq. (9), the following ansatz can be used:

$$\mathbf{q}'(x,y,z,t) = \mathbf{q}(x,y,z)e^{\mathrm{i}\left(\int_{x_{0,d}}^{x}\alpha(\xi)\mathrm{d}\xi-\omega t\right)} + \text{c.c.}, \tag{11}$$

where $x_{0,d}$ is the upstream location from which the disturbance originate, and $\xi$ is the dummy variable of the integration. Substituting Eq. (11) into Eqs. (7)–(8), the plane-marching PSE can be derived:

$$\mathbf{A}\mathbf{q} + \mathbf{B}\frac{\partial\mathbf{q}}{\partial y} + \mathbf{C}\frac{\partial^2\mathbf{q}}{\partial y^2} + \mathbf{D}\frac{\partial\mathbf{q}}{\partial z} + \mathbf{E}\frac{\partial^2\mathbf{q}}{\partial z^2} + \mathbf{F}\frac{\partial\mathbf{q}}{\partial x} = 0. \tag{12}$$

The terms of the matrices can be found in [69]. Eq. (12) can be solved, starting from a suitable initial condition that is obtained by solving the BiGlobal stability equations, marching downstream.

The solution of the PSE is, without additional details, ambiguous, since both the shape function $\mathbf{q}$ and the phase through $\alpha$ varies in the streamwise direction. The ambiguity can be resolved by enforcing the following constraint:

$$\int_0^{y_{\max}}\int_{z_{\min}}^{z_{\max}}\mathbf{q}^*\frac{\partial\mathbf{q}}{\partial x}\mathrm{d}y\mathrm{d}z = 0, \tag{13}$$

which enforces that all the exponential variation $\mathbf{q}'$ is contained in the complex streamwise wavenumber $\alpha$. In the equation above, $^*$ denotes the conjugate transpose. Eq. (13) can be satisfied by iteratively updating $\alpha$, which was done using the formula suggested by Herbert [71]:

$$\alpha_{k+1} = \alpha_k - \mathrm{i}\frac{\int_0^{y_{\max}}\int_{z_{\min}}^{z_{\max}}\mathbf{q}_k^*\frac{\partial\mathbf{q}_k}{\partial x}\mathrm{d}y\mathrm{d}z}{\int_0^{y_{\max}}\int_{z_{\min}}^{z_{\max}}\mathbf{q}_k^*\mathbf{q}_k\mathrm{d}y\mathrm{d}z}. \tag{14}$$

In the case of the PSE, the growth rate of various flow variables are different [71]. In our study, the energy-based growth rate is used:

$$\mu_E = -\alpha_i + \frac{\partial}{\partial x}\ln\left(\sqrt{E}\right), \tag{15}$$

where

$$E = \int_0^{y_{\max}}\int_{z_{\min}}^{z_{\max}}\left(uu^* + vv^* + ww^*\right)\mathrm{d}y\mathrm{d}z. \tag{16}$$

The transition to turbulence is predicted using the $e^N$ method [59] in which the transition location is assumed to correlate with the $N$ factor:

$$N_j = \max_F\left[\int_{x_{j,1}}^{x_{j,2}}\mu_j(F,x)\mathrm{d}x\right], \tag{17}$$

where $j$ is the index of the eigenmode (if there is more than one) $x_1$ is the first streamwise location where instability occurs, and $x_2$ where the maximum growth is reached; both depend on the frequency. The transition is assumed to occur when a prescribed value of $N$ is reached. The instability waves were separated into two categories based on previous studies [25,27,29]: the modified TS waves, and the secondary instabilities. TS waves, being the primary instability mechanism in the two-dimensional boundary layer, are attenuated by the streaks, and trigger transition at low frequencies. Secondary instabilities, on the other hand, arise due to the presence of the streaks. They are unstable in a broad frequency interval, and are dangerous as they can potentially advance transition. The two classes of instabilities were treated differently in both the transition prediction, and also in the numerical computations (see Section 2.3).

In the case of TS waves, $N = 7$ was used for the transition prediction, which can be considered a very conservative estimate [59]. However, in the case of the secondary instabilities, no $N$ value is available for transition prediction. Therefore, the maximum $N$ value is calculated for each unstable mode, and the highest $N$ value among the modes is used to quantify the destabilisation of the boundary layer. As will be discussed later, tracking and separating the individual unstable modes requires a very fine streamwise resolution. Thus, an insufficient streamwise resolution makes the distinction of the unstable modes challenging. To avoid the very large computational cost associated with a fine streamwise resolution, as an alternative, the $N$ factor was also evaluated in the case of secondary instabilities with the most unstable mode of the eigenvalue spectrum, taken at each streamwise location and frequency. The utilisation of this alternative $N$ factor allows the computation to be more automated, which is also desirable for large scale parametric studies and optimisation. This alternative $N$ factor is denoted with $N_{\mathrm{MU}}$ (Most Unstable), and the reliability of the proposed method will be discussed in Section 3.

### 2.3. Numerical solution and parameters

The base flow computation consists of two steps: calculation of the flow field near the MVG using 3D CFD, and the calculation of the flow downstream of the MVG by solving the BRE. The geometry consists of a rectangular box around the MVG (brown in Fig. 1(a)). The parameters of the computational domain are essentially the same as Siconolfi et al. [29]. The computational domain starts at $\hat{x}_0$, ends at $\hat{x}_{1,\mathrm{CFD}}$ (not shown in the figure), and the location of the MVG, defined by its centre, is $\hat{x}_{\mathrm{MVG}}$; see also Table 1 and Fig. 1(a). In terms of the boundary layer thickness, the distance between the MVG location and the upstream and downstream ends of the computation domain is $2.49\hat{\delta}_{99,\mathrm{MVG}}$ and $4.98\hat{\delta}_{99,\mathrm{MVG}}$, respectively. The BRE calculation is initialised at $\hat{x}_{\mathrm{st}}$, slightly upstream of the end of the computational domain, so that the downstream boundary conditions do not influence the velocity profile from which the BRE is initialised. Finally, the height of the computational domain was 13 mm in all the computations. Note that we examine MVGs whose height is 1.5 times the highest MVG investigated by Siconolfi et al. [29]. However, in a preliminary study, Camarri et al. [72] examined the size of the computational domain, and found that its effect is not significant. Therefore, although we did consider changing the size of the computational domain, were convinced that its parameters are reasonable.

The base flow near the MVG is obtained using the commercial CFD code ANSYS CFX 21 R2 [73], which uses the finite volume method to solve the Navier–Stokes equations. To obtain the equilibrium solution, the steady-state solver was used. Furthermore, to reduce the size of the problem, only half of the geometry (only a single MVG) was present in the computations, and the rest of the computational domain was accounted for by prescribing the symmetry of the base flow. This consideration significantly speeds up the computations (they takes roughly two hours on a desktop computer). However, both of the above choices suppress the development of instabilities. Therefore, we did not check for global instabilities implicitly in the base flow calculation, like Siconolfi et al. [29], who used DNS to calculate the base flow on the entire geometry. The global instability of the MVGs should be investigated in a future study. The remaining boundary conditions are the following. At the other spanwise boundary, again the symmetry of the base flow was prescribed. At the upstream boundary, a Blasius boundary layer was considered. At the downstream end of the computational domain, a free-outflow (zero normal stress) boundary condition was applied. Finally, on the top of the domain, a so-called entrainment boundary condition was used, which allows both in- and outflow to the computational domain with imposing a 0 static pressure, and zero velocity gradient perpendicular to the boundary [73]

A fully parametric structured mesh has been created using the program GMSH [74]. The mesh used for the base configuration is displayed

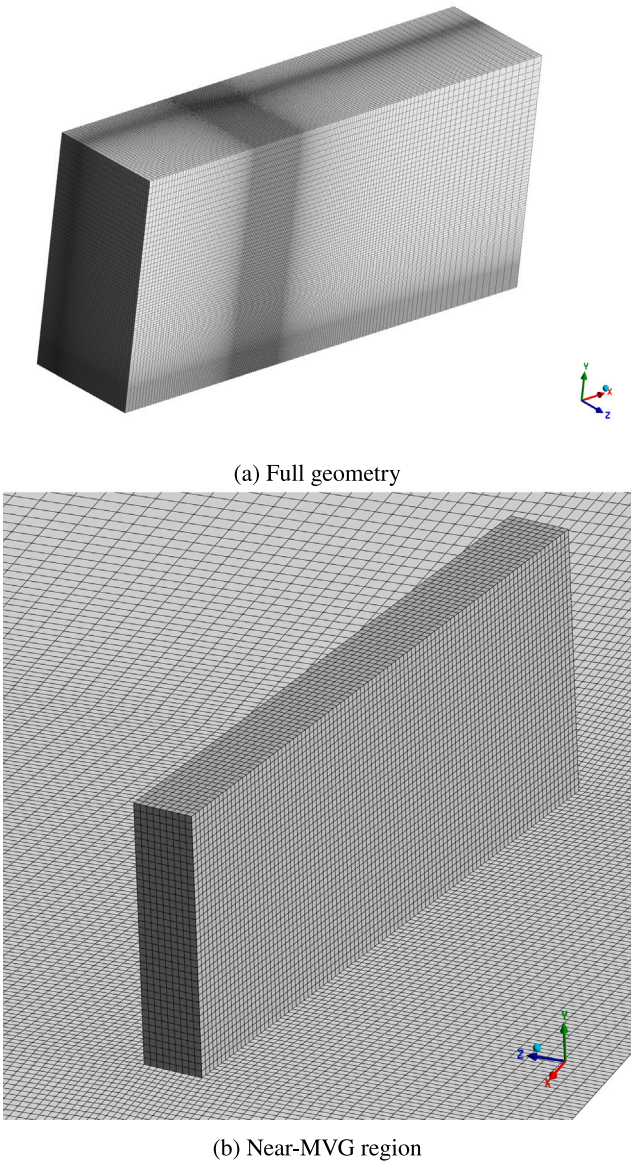

(a) Full geometry

(b) Near-MVG region

**Fig. 2.** The mesh used in the CFD calculation of the base configuration.

in Fig. 2. In the parametrisation, exceptional care has been taken to avoid large mesh size variations and angles. It is clearly displayed in the figure that the mesh near the MVG is the finest, and moving away from it the element size progressively increases. The shortest edge of the MVG ($\hat{w}$) is divided into 9 elements, which gives a minimum cell size of 0.0333 mm ($0.0092\hat{\delta}_{99,\mathrm{MVG}}$). The typical mesh consisted of roughly $3 - 5 \cdot 10^6$ elements. An RMS residual target of $10^{-9}$ was reached in the iterative solution of the governing equations. Second order spatial discretisation was used, and it was checked that increasing the mesh resolution has a negligible effect on the results.

The BRE, BiGlobal stability equations and PSE are solved using the finite elements method. The parallel-version of the open-source finite element library FreeFem [64] was used for the problem solution. Taylor-Hood elements are used: the velocity and pressure fields are discretised using $\mathcal{P}_2$ and $\mathcal{P}_1$ elements, respectively. This discretisation is very common in global stability analysis of two- and three-dimensional flows. In the parallel version of FreeFem, the mesh is decomposed into multiple overlapping parts, and a mesh region is assigned to each processor along with the corresponding degrees of freedom. The mesh consisting of triangular elements is created using BAMG [75],

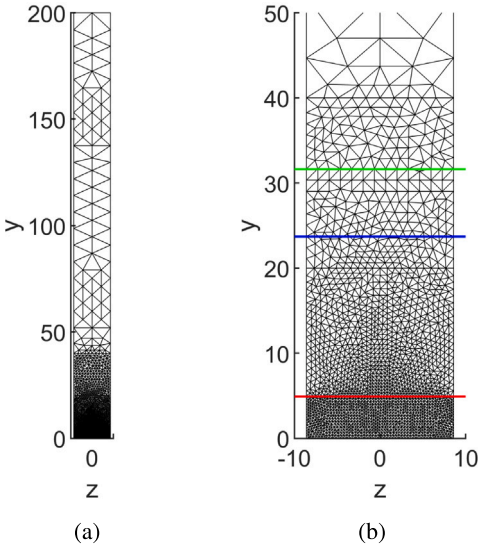


**Fig. 3.** A typical mesh used in the BRE and BiGlobal stability calculations. (a): Full mesh. (b): Zoomed mesh. The red, blue and green lines display the boundary layer thickness $\delta_{99}$ at the start of the computation ($\mathrm{Re}_\delta = 310.69$), $\mathrm{Re}_\delta = 1500$ and 2000, respectively.

the build-in mesh generator of FreeFem which meshes the geometry using Delaunay triangulation. The mesh consists of multiple blocks, each with different element size specification along the edges. A typical mesh is displayed in Fig. 3. In Fig. 3(a), the separate regions with different mesh sizes can be distinguished. It stands out that very large elements can be used in the far field. In Fig. 3(b), the mesh region close to the wall is highlighted. Here, the red, blue and green lines denote the boundary layer thickness $\delta_{99}$ at three different locations. The first one is at $\hat{x}_{\mathrm{st}}$, where the BRE solution is started. The second is at $\mathrm{Re}_\delta = 1500$, roughly where the Blasius boundary layer transitions to turbulence, based on the solution of the Orr–Sommerfeld equation and the $e^N$ method with $N = 7$. The last streamwise position is at $\mathrm{Re}_\delta = 2000$, beyond which transition could not be postponed within the investigated MVG parameter set. Comparison of the line positions with the element size it can be concluded that the mesh is sufficient to resolve the variation of the base flow and the instabilities along the whole streamwise domain considered. It was also checked that increasing the mesh resolution did not alter the results; e.g., doubling the number of triangles changed the transition Reynolds number by less than 0.1%. The other meshes are also deemed to have sufficient resolution, since the meshes used for each investigated case only differ in the spanwise domain size; the element-size distribution is the same.

The BRE are discretised with a second order backward Euler scheme in the streamwise direction, except for the first step, where the first order backward Euler method was used. The spatial stepsize of the BRE is chosen the following way. The streamwise domain is divided into 100 intervals, so that the square root of the streamwise stations is equidistant, to follow the faster variation of the flow in the upstream region. The upstream part is further refined: the first 8 intervals are halved; then, repeated 6 times, always the current first 32 intervals halved. This resulted in $\approx 300$ steps, ensuring that the upstream region of the streaky boundary layer, where the variation of the flow is more rapid, is sufficiently resolved.

The equations were solved using the sparse linear algebra library PETSc [65,66] and eigenvalue solver SLEPc [67]. The nonlinear system of equations that arise from the discretisation of the BRE was solved using a second order line search (Newton–Raphson) method with the SNES library of PETSc. The inversion of the Jacobian was done with LU factorisation using the sparse linear algebra solver MUMPS [76,77]. The absolute tolerance of the nonlinear equations solution was $5 \cdot 10^{-13}$, the relative tolerance was $5 \cdot 10^{-13}$, or the norm of the change in the solution is less than $10^{-4}$. For a precise definition of the tolerances, the reader is referred to the PETSc manual [66]. The solution of the BRE takes a short time, compared to both the 3D CFD and the stability calculations.

The parameters of the eigenvalue calculation are explained in the light of the fact that an extreme amount of eigenvalue calculations were performed: for each MVG configuration, streamwise location and frequency, the relevant part of spectrum had to be calculated.

For the numerical solution of the BiGlobal spatial stability equations the SLEPc PEP library [78] was used, which requires only the coefficient matrices of the polynomial eigenvalue problem. Since the calculation of the entire eigenvalue spectrum with QR factorisation is not feasible, the iterative Krylov-Schur algorithm combined with the shift invert technique, similarly to Siconolfi et al. [29] was applied. The matrix inversion was calculated using the MUMPS solver, similarly to BRE. This technique allows the calculation of the eigenvalues close to an initial guess, called the shift. Every BiGlobal stability calculation (which is required for each MVG configuration, streamwise location and frequency) multiple eigenvalue calculations with different shifts were used to determine the relevant part of the eigenvalue spectrum. The shifts were determined based on the following three arguments:

(i) For downstream travelling convective instabilities, the (nondimensional) phase speed ($c_p$) is typically in the interval $c_p \in [0.1, 0.95]$; solutions of the BiGlobal instability problem outside this interval (if upstream travelling waves are not considered) can be deemed irrelevant. Based on the phase speed, an interval can be calculated for the real part of the streamwise wavenumber. This constraint can also be used to select the non-physical or irrelevant eigenvalues.

(ii) In boundary layer flow, in general, $|\alpha_i| < |\alpha_r|$. Therefore, in the above specified region, the eigenvalues of interest are close to the real axis.

(iii) It was shown by numerical stability analysis of streaky boundary layers [27,29] that instabilities can be separated into two classes: the modified TS waves, and secondary instabilities. TS waves according to the $e^N$ theory, trigger turbulence at a low frequency relatively far downstream. Secondary instabilities, on the other hand, are broadband instabilities, which are located downstream of the MVG wake, or at the maximum amplitude region.

All these criteria were used for an efficient eigenvalue calculation. As mentioned in the previous section, for each MVG configuration, two sets of BiGlobal stability calculations were conducted: one targeting the secondary broadband instabilities that arise because of the MVG or streaks and one the (modified) TS waves. Within each run, for each frequency, the eigenvalues were monitored by repeated solutions of the BiGlobal instability problem, marching downstream. The eigenvalues were paired between successive streamwise locations by comparing both the eigenvalues and eigenfunctions.

The parameters of the two runs are displayed in Table 2. $F$ and $\Delta F$ denote the nondimensional frequency parameter range, where $F = \hat{\omega}\hat{\nu}/\hat{U_0}^2 \cdot 10^6$. The frequency intervals were chosen based on the data presented by Siconolfi et al. [29], and the well-known stability characteristics of TS waves. $F_{\mathrm{init}}$ is the first frequency in each run. First, the stability calculation is run at this frequency, and the streamwise computational domain is truncated slightly downstream of the location after which no unstable eigenvalue was found. This frequency is chosen to be the lowest in the case TS waves, based on their neutral curve. In the case of the secondary broadband instabilities, the initial frequency is chosen so that it does not miss any unstable modes; the reliability of this choice is discussed in Section 3.3. For the secondary instabilities, two values are displayed: they were used to calculate the modelling of the experiments of Sattarzadeh and Fransson [22] (Section 3.1) and the parametric study (Section 3.3), respectively. This is because after the

**Table 2**
Parameters of the BiGlobal stability calculations.

| Parameter | Secondary broadband | TS |
|---|---|---|
| $F$ | [60, 300] or [100, 400] | [10, 50] |
| $\Delta F$ | 15 or 20 | 5 |
| $F_{\text{init}}$ | 105 or 200 | 10 |
| $c_p$ | [0.2, 0.4, 0.6, 0.8] | 0.3 |
| $n_{\text{EV}}$ | [20, 15, 15, 15] | 10 |
| $n_{\text{Kryl}}$ | $3 \cdot n_{\text{EV}}$ | $3 \cdot n_{\text{EV}}$ |
| $n_{\text{iter}}$ | [10, 7, 7, 7] | 10 |

fist set of calculations, the parameters were adjusted to better capture the physical phenomena and for increased robustness.

In the case of secondary instabilities, multiple phase speeds (shifts - eigenvalue guesses) are used to target the physically relevant part of the eigenvalue spectrum; in the case of TS waves, only a single shift is used to target the TS waves only - no additional unstable modes are expected. The phase speeds determine the real part of the shifts, and the imaginary parts of the shifts are zero. $n_{\text{EV}}$, $n_{\text{Kryl}}$ and $n_{\text{iter}}$ denote the number of requested eigenvalues, the Krylov subspace dimension, and the maximum number of iterations — the solver stops, if either the number of requested eigenvalues or the maximum iteration number is reached.

The above setting proved to be sufficient to find any mode that becomes unstable. However, since the shifts are located close to the imaginary axis, with these settings sometimes the imaginary part of an eigenvalue became so negative (very unstable mode) that it was lost in the tracking procedure, while marching downstream. Therefore, as a remedy, in the case of a lost unstable eigenvalue, an additional shift was added with the previous value of the most unstable mode. The above options allowed a reliable scanning of the instability domain.

Concluding the discussion of the numerical methods, the plane marching PSE is reviewed. In the streamwise direction, second order backward-Euler method was used, except for the first step, in which first order backward-Euler is utilised. The streamwise domain was divided into 30 and 70 parts in the case of the secondary sinuous instability and the TS waves, respectively, so that the square root of the streamwise coordinate is equidistant. In each marching step, until the absolute value of the integral in Eq. (13) was smaller than $10^{-7}$, $\alpha$ was updated iteratively with formula Eq. (14).

## 3. Results

In this section, the results obtained from the previously outlined modelling framework are presented. First, in Section 3.1, the experiments of Sattarzadeh and Fransson [22] are modelled, and a detailed comparison between our simulations and their measurements is presented. Then, in Section 3.2, the streaky base flow, particularly the streak amplitude is discussed in the case of the parametric study. Finally, in Section 3.3, also for the parametric study, the results of the stability calculations are presented.

The parametric study of the streaky base flow is performed on a parameter grid $\hat{h} = [1.3 : 0.2 : 1.9]$ mm ($[0.360 : 0.0554 : 0.526]$ $\hat{\delta}_{99,\text{MVG}}$), $\hat{\Lambda} = [7 : 3.25 : 26.5]$ mm ($[1.949 : 0.900 : 7.34]$ $\hat{\delta}_{99,\text{MVG}}$), $\hat{d}/\hat{\Lambda} = [0.2 : 0.075 : 0.8]$, where the values in the brackets define the first point, the spacing, and the last point of the parameter grid. This results in a total of 252 cases. The data are only shown for a selected subset of cases to show the key observations. Then, the stability calculations were run only on a coarser grid of $\hat{d}/\hat{\Lambda} = [0.2 : 0.15 : 0.8]$, since this is the most computationally demanding task in the modelling framework. This choice narrows the number of cases to 140. Note that the single other study concerned with the stability characteristics of realistic MVG geometries, conducted by Siconolfi et al. [29], presented results for only two cases.

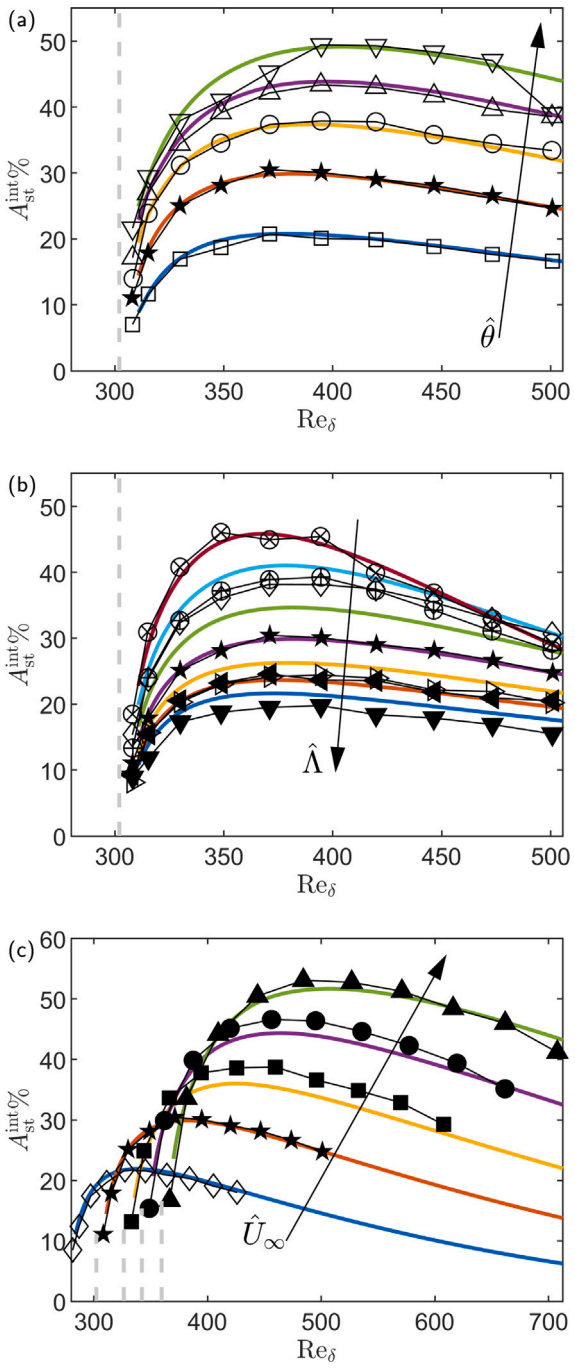


**Fig. 4.** Integral streak amplitude as a function of the Reynolds number: comparison between the simulation and the experiments of Sattarzadeh and Fransson [22]. The symbols and coloured lines denote the experimental data and the numerical calculations, respectively; the dashed vertical lines denote the location of the MVG. The symbol ⋆ denotes the base case (Table 1). a: $\hat{\theta} \in [6, 9, 12, 15, 18]$ (°), b: $\hat{\Lambda} \in [8.13, 9.75, 11.38, 13.00, 14.63, 16.25, 17.88]$ (mm), c: $\hat{U}_\infty \in [5, 6, 7, 7.7, 8.5]$ (m/s).

### 3.1. Validation and general observations: modelling the experiments of Sattarzadeh and Fransson [22]

In this section, the simulations modelling the experiments of Sattarzadeh and Fransson [22] are discussed. First, the streak amplitude evolution is compared with experimental data; then, the results of the stability calculations are presented.

Fig. 4 displays the comparison of the integral streak amplitude between simulation and experiments. The symbols and coloured lines

denote the experimental data and the numerical calculations, respectively; the dashed vertical lines denote the location of the MVG. In each subfigure, a single parameter is varied: in Figs. 4(a), 4(b) and 4(c), $\theta$, $\Lambda$ and $U_\infty$ are altered, respectively. The arrows indicate the change in the parameter, and the parameter values can be found in the caption.

Examining Fig. 4(a) where $\hat{\theta}$ is varied, a remarkably good agreement can be found between the experimental data and the simulations. Notable discrepancy can only be seen in the case of $\hat{\theta} = 18°$ (green curve). At $\mathrm{Re}_\delta = 500$, the difference is attributed to the boundary layer becoming turbulent in the experiments due to the large separation associated with the strong wake because of the large MVG angle - a phenomenon that cannot be captured in the present model. Also for $\hat{\theta} = 18°$, at $\mathrm{Re}_\delta \approx 350$, the trend of the experimental streak evolution is slightly different from the other cases, for which no indication is given by the experimentalists. It is possible that the discrepancy can be attributed to the temporal variation of the flow, which cannot be captured in our model. Either an absolute instability in the wake, or a transient growth of the disturbances impinging on the MVGs can cause a significant flow distortion. This is supported by the fact that the flow became turbulent at $\mathrm{Re}_\delta = 500$ in the experiments. Nevertheless, it can be concluded that this set of experiments could be modelled by the numerical simulations outstandingly well.

In Fig. 4(b), the streak amplitude comparison is shown when the spanwise periodicity $\hat{\Lambda}$ is changed. In this case, the agreement between simulation and experiments is satisfactory but not outstanding. For $\hat{\Lambda} = 8.13$ mm (⊗ - dark red), $\hat{\Lambda} = 13.00$ mm (⋆ - purple), and $\hat{\Lambda} = 16.25$ mm (► - orange), the simulations match the experiments, while in the rest of the cases, noticeable discrepancies can be found. Although the experimentalists were extremely precise, the disagreement might be attributed to the large spanwise spacing (0.6–1 mm) of the measurement locations. The ⊕ − ▽ and ◄ - ▷ curves are very close in the experiments. This is attributed to the destructive–constructive and constructive-no interaction of the counter-rotating vortex pairs as the spanwise distance is increased. Contrary to these experimental observations, in the simulations, a continuous dependence of the amplitude curve on $\hat{\Lambda}$ can be found. We note that the lift-up, the mechanism that creates the streaks from the streamwise vorticity, is an extremely effective mechanism: a very small streamwise vorticity can create a very large downstream response [79]. A small mean flow distortion (MFD) induced by either absolute instability or transient growth of convective instabilities, or a discrepancy in the geometry because of uncertainties, can cause a large difference in the streaky flow. The precise reason for the difference between experiments and simulations is unclear.

The last set of streak amplitude comparison with the experiments is presented in Fig. 4(c), for a variation of the streamwise velocity. Note that although in the experiments the location of the MVGs on the flat plate was constant, since $\mathrm{Re}_\delta$ is used as streamwise coordinate, due to the nondimensionalisation the MVGs appear at different streamwise locations. In this case, the simulations match the experimental amplitude curves very well. Note that the simulations predict a slower decay of the streaks compared to the experiment. This is likely because the BRE are less dissipative due to the neglecting of the second streamwise derivates. This was also noted by Martín and Paredes [27] when comparing their streak amplitudes calculated using BRE with the DNS results of Siconolfi et al. [25], modelling streaks induced by free-stream vortices.

Overall, based on the comparison with the experiments, it can be concluded that the simulations model the streaky base flow satisfactorily. This is especially true, considering that Siconolfi et al. [29] reported slightly worse agreement in their simulations of MVG wind tunnel experiments. They calculated the base flow with a spectral DNS solver, and modelled only two triangular MVG configurations from the experiments of Shahinfar et al. [17].

Next, our attention is turned to the BiGlobal stability calculations. First, the characteristics of the instability calculations are illustrated on a single case; then, the results are presented in a more compact way for all the experimental cases. An illustration of the stability calculations is presented in Fig. 5, for the case when the free stream velocity is $\hat{U}_\infty = 7.7$ m/s (case C10 in [22]). In these figures, the growth rate of the most unstable mode is displayed as a function of Re and $F$, the solid lines separate the stable and unstable domains of the individual modes, and the dashed line displays the neutral curve of the TS waves in the Blasius boundary layer obtained from the solution of the Orr–Sommerfeld equation. Fig. 5(a) displays the total instability map, in which the two calculations targeting the broadband secondary instabilities and the TS waves can be clearly distinguished. The two sets of calculations are also displayed independently in Figs. 5(b) and 5(c), respectively. It stands out from the figures that since our approach focuses on the physically relevant portion of the $\mathrm{Re}_\delta - F$ plane, a large body of unnecessary calculations is omitted which speeds up the computational procedure substantially.

Focusing on the secondary instabilities presented in Fig. 5(b), it can be seen that on a relatively short streamwise interval, several different unstable modes emerge due to regions with strong shear that are induced by the MVGs. This is where the tracking of the individual unstable modes is problematic since it requires a fine streamwise discretisation, for which the alternative $N_{\mathrm{MU}}$ has been proposed. Note that the secondary instabilities are relevant on a much shorter streamwise interval than the TS waves, which applies to all the calculations. Moving on the TS wave stability diagram in Fig. 5(c), the stabilising effect of the MVGs is clearly visible when the neutral curves of the unaltered (dashed curve) and streaky boundary layer (grey curve) are compared. As apparent from the figure, the region upstream of $\mathrm{Re}_\delta = 800$ is not well resolved. The reason for this is that since the calculations target specifically the TS waves, only a single eigenvalue guess was used in the shift-invert procedure. This follows from the fact that the secondary instabilities are relevant at high frequencies. In all the calculations, the TS waves could be easily and automatically separated from unresolved low frequency secondary instabilities.

Next, using the $e^N$ method, the results of the BiGlobal stability calculations for all the modelled experimental configurations are presented in Fig. 6. The left axis (blue) shows the two $N$ factors used to characterise the secondary instabilities. The continuous and dashed lines denote the $N$ factor of the most destabilising mode, and the proposed $N_{\mathrm{MU}}$ that is calculated from the most unstable eigenvalue of the spectrum, respectively (see the end of Section 2.2 for a more detailed description). High $N$ values are the sign of strong destabilisation and are, therefore, not desired. The right axis (red) displays the transition Reynolds number calculated from the modified TS waves, using a conservative $N = 7$ value for the transition prediction. Good MVGs are indicated by high values of $\mathrm{Re}_{\mathrm{Tr}}$. The red axis starts at $\mathrm{Re}_{\mathrm{Tr}} \approxeq 1500$ where transition is predicted by the Orr–Sommerfeld equation, and the horizontal dotted line ($\mathrm{Re}_{\mathrm{Tr}} \approxeq 1540$) displays the same quantity calculated from the BiGlobal stability equations. This difference can be attributed mainly to the non-parallel terms in the BiGlobal stability equations that are omitted from the Orr–Sommerfeld equations.

Comparing the two measures of destabilisation, it is clear that the proposed $N_{\mathrm{MU}}$ factor follows the same trend as the regular one. Furthermore, the overprediction of the $N_{\mathrm{MU}}$ factor is not significant, except for one point in each figure: at $\hat{\theta} = 8°$, $\hat{\Lambda} = 8.13$ mm, and $\hat{U}_\infty = 5.5$ m/s in Fig. 6(a), 6(b) and 6(c), respectively. This can be attributed to the following. In these cases, the boundary layer modulation is weak (see Fig. 4); therefore, the TS waves remain unstable at high frequencies. Because of this, TS waves provide some contribution to $N_{\mathrm{MU}}$; on the other hand, TS waves are not considered in the secondary instability calculations and thus, in the calculation of $N$. Overall, the agreement between $N$ and $N_{\mathrm{MU}}$ can be considered excellent.

Meaningful comparison of the local modal stability calculations with experimental amplification factors is limited for three reasons. First, the TS waves were excited upstream of the MVG in the experiments; therefore, the experimental $N$ factors include the contribution

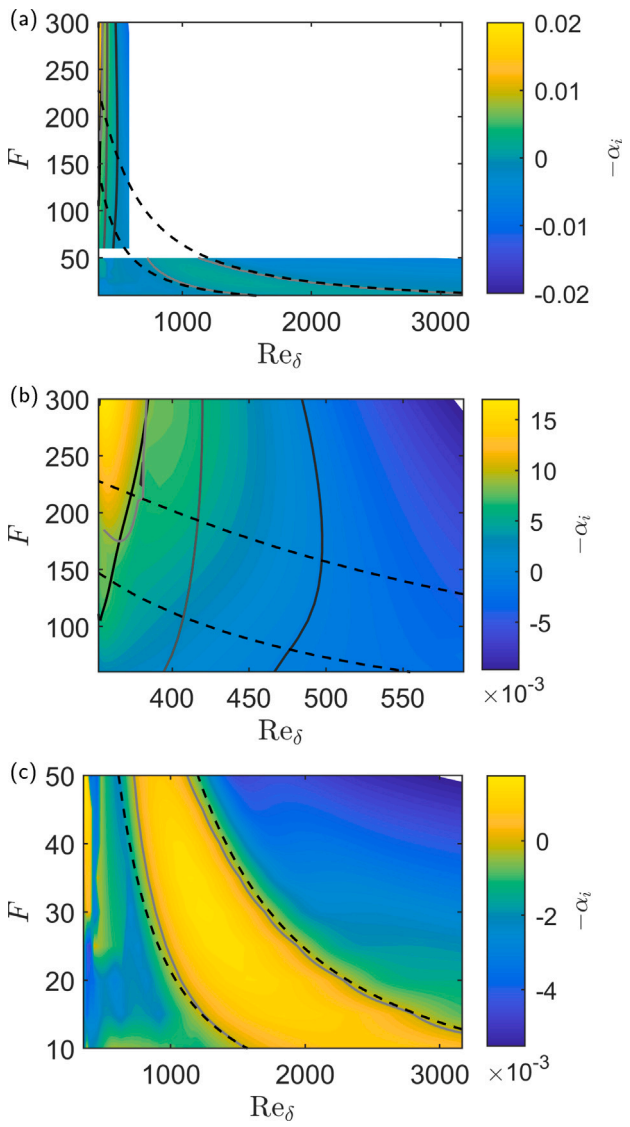


**Fig. 5.** Most unstable growth-rate as a function of $\mathrm{Re}_\delta$ and $F$, for the experiments of Sattarzadeh and Fransson [22] with free-stream velocity $\hat{U}_\infty = 7.7$ m/s (case C10 in their paper). The solid lines display the neutral curves of the individual unstable modes, the different shades denote separate modes; the dashed line displays the neutral curve of the undisturbed Blasius boundary layer. a: total $\mathrm{Re}_\delta - F$ plane; b: high-frequency secondary disturbances; c: TS waves.

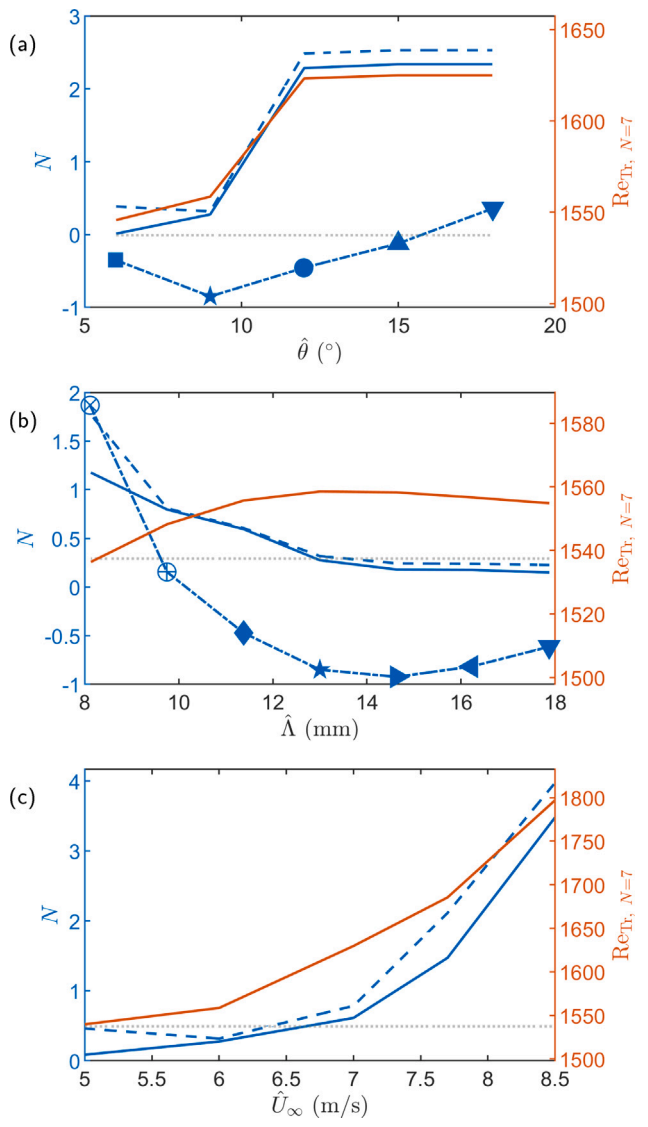


**Fig. 6.** Stability calculations of the experiments of Sattarzadeh and Fransson [22]. Maximum $N$ factor of the secondary instabilities (blue), and transition Reynolds number (orange) as functions of the geometric parameters of the MVG. The grey dotted line denotes the transition Reynolds number in the undisturbed Blasius boundary layer. The dashed blue line denotes the $N_{\mathrm{MU}}$ factor calculated with the maximum growth rate among the individual modes at each spatial location and frequency. The blue curves with the symbols denote the experimental $N$ factors measured by Sattarzadeh and Fransson [22]. The variables are the following: a: $\hat{\theta}$; b: $\hat{\Lambda}$; c: $\hat{U}_\infty$.

from the fully three-dimensional flow around the MVG, while the stability calculation is performed downstream of the MVGs. Second, the experimental $N$ factor contains contribution from many modes simultaneously, while local modal stability analysis uses a single growth rate at a time. Third, the experimentalists measure the amplification at a single frequency, which is not expected to match the frequency of maximum amplification in the stability analysis. Nevertheless, for a qualitative comparison, the dash-dotted curves with the symbols display the experimental $N$ curves in Figs. 6(a) and 6(b). Unexpectedly, both the $N$ and $N_{\mathrm{MU}}$ curves of the stability calculation correlate well with the experimental $N$ factors. Interestingly, the $N_{\mathrm{MU}}$ factor seems to correlate better with the experimental results. This suggests that local modal stability analysis can provide recommendations for the restriction of the large parameter space of all possible MVG configurations. Of course, for superior performance, non-local, non-modal, and possibly also non-linear effects need to be analysed.

Next, the evolution of the TS waves is analysed by examining the transition Reynolds number $\mathrm{Re}_{\mathrm{Tr}}$, displayed with the red curves in Fig. 6. Here, unfortunately, comparison with the experiments is not relevant, since the presented calculation analyses the stability of TS waves in the frequency range $F \in [20 - 40]$, where transition is predicted by the $e^N$ method. On the other hand, the experimentalists used higher frequencies, a choice which was possibly motivated by the streamwise extent of the measurement domain. In Fig. 6(a), where the effect of varying $\hat{\theta}$ is displayed, two regions with different behaviour can be distinguished. First, as the angle is increased, TS waves get more stabilised. This is because MVGs with larger angle generate a stronger streamwise vorticity, which create stronger streaks. However, further increasing the MVG angle does not increase the stabilisation further. This can be explained as increasing $\hat{\theta}$ increases the breadth of the wake behind the MVG but does not add more streamwise vorticity that can generate long-lasting streaks through the lift-up mechanism.

Turning our attention to the effect of $\hat{\Lambda}$ on $\mathrm{Re}_{\mathrm{Tr}}$, displayed in Fig. 6(b), it stands out that for this MVG configuration, the variation

of $\hat{\Lambda}$ has insignificant influence on the stability of low frequency TS waves. This is because in all these cases, the streaks decay fast and do not extend far downstream (see Fig. 4(b)). Finally, as it can be observed in Fig. 6(c), by increasing the free-stream velocity the transition significantly moves downstream. This can be explained by the fact that increasing the free-stream velocity reduces the boundary layer thickness, therefore the ratio $\hat{h}/\hat{\delta}$ is also increased. This results in generation of stronger vortices, and streaks that extend further downstream.

### 3.2. Parametric study: evolution of the streaky boundary layer

In Fig. 7 the three columns display the integral streak amplitude, the maximum difference based streak amplitude, and the relative skin friction difference compared to the Blasius boundary layer, respectively, for a MVG height $\hat{h} = 1.3$ mm. These quantities are depicted as functions of $\mathrm{Re}_{\hat{\delta}}$ and $\hat{d}/\hat{\Lambda}$. The rows of figures correspond to different values of $\hat{\Lambda}$. $\hat{d}/\hat{\Lambda} = 0.5$ corresponds to equidistant MVG pairs, closely spaced MVGs ($\hat{d}/\hat{\Lambda} \approx 0.2$ were the most investigated ones [16,17,22]. Note that due to the symmetry of the configuration, $\hat{d}/\hat{\Lambda} = 0.8$ corresponds to the same orientation as $\hat{d}/\hat{\Lambda} = 0.2$, but with a reversed flow direction.

First, the effect of changing the spanwise periodicity $\hat{\Lambda}$ is analysed. This is the same in the case of both amplitude definitions: increasing $\hat{\Lambda}$ reduces the initial amplitude maximum, but increases the amplitude of the streak far downstream. These results agree with the observations of studies that focused on idealised vortices [28,79]. This can be attributed to vortex interaction: at high $\hat{\Lambda}$, the larger spacing delays the streak generation, which results in more elongated streaks with lower maximum amplitude. Because of the weaker initial interaction, the depletion of the streamwise vorticity is slower, and the lift-up mechanism can act further downstream, resulting in stronger streaks there. Large values of $\hat{\Lambda}$ are, therefore, desirable for flow control, since (i) they avoid the high initial amplitudes that may result in secondary instabilities and premature transition, and (ii) they yield persistent streaks that are able to attenuate the TS waves far downstream. Although this is not a fundamentally new result, we stress its importance as this is not apparent in the experiments of Sattarzadeh and Fransson [22] (see also Fig. 4(b)).

Next, the effect of changing $\hat{d}/\hat{\Lambda}$ is discussed. In the downstream part of the investigated domain, the two streak amplitudes show the same trend: the highest downstream streak amplitudes can be observed near $\hat{d}/\hat{\Lambda} \approx 0.5$. Note that studies of optimal vortices [79] also predict this vortex spacing to generate the strongest streaks. Optimal vortices are spanwise periodic, equidistant counter-rotating vortices, which are known to produce the largest disturbance energy growth measured at a streamwise location, from a unit input disturbance energy introduced at some other location. The results in the figure suggest that the equidistant spacing suggested by the optimal vortices is also applicable to the 'non-ideal' vortices generated by the MVGs to dampen the TS wave growth.

The trends described by the two streak amplitudes agree in the upstream part of the domain for low $\hat{\Lambda}$: the highest near field amplitude is always predicted in the interval $\hat{d}/\hat{\Lambda} \in [0.4 - 0.6]$. In contrast, when $\hat{\Lambda}$ is increased, the behaviour of the two streak amplitudes is qualitatively different. In the region $\hat{d}/\hat{\Lambda} \in [0.3 - 0.6]$, roughly where previously the maximum $A_{\mathrm{ST}}^{\mathrm{diff}}$ could be found, the lowest peak amplitudes can be observed. Meanwhile, the maximum $A_{\mathrm{ST}}^{\mathrm{int}}$ value in the upstream region remains roughly at the same values of $\hat{d}/\hat{\Lambda}$. In addition to the qualitative changes, note that the values of the streak amplitude are also different: the maximum value of $A_{\mathrm{ST}}^{\mathrm{int}}$ is almost twice as high as that of $A_{\mathrm{ST}}^{\mathrm{diff}}$.

Before investigating the differences between the two streak amplitude definitions in more detail, the effect of changing the MVG height $\hat{h}$ is analysed. Fig. 8 is the same as Fig. 7 but for an MVG height $\hat{h} = 1.9$ mm. The same trends can be observed in Fig. 8 as in Fig. 7 with respect to both the variation of $\hat{\Lambda}$ and $\hat{d}/\hat{\Lambda}$, except for two things. First, the maximum value of $A_{\mathrm{ST}}^{\mathrm{diff}}$ is shifted to $\hat{d}/\hat{\Lambda} \approx [0.2 - 0.5]$ at low values of $\hat{\Lambda}$; then, similarly to $\hat{h} = 1.3$ mm, as $\hat{\Lambda}$ is increased, the previous region of maximum amplitude is smeared. Second, in the case of both $A_{\mathrm{ST}}^{\mathrm{int}}$ and $A_{\mathrm{ST}}^{\mathrm{diff}}$, significantly higher streak amplitudes can be observed in Fig. 8. As expected, increasing the MVG height results in a more pronounced vortex generation and therefore, stronger streaks; this agrees with the findings of Sattarzadeh and Fransson [22] (see also Fig. 4(c)). Results are not presented for the remaining two MVG heights since they display the same tendencies as Figs. 7 and 8.

To gain more insight into the differences between the two streak amplitudes, more detailed data are presented on the streaky boundary layer for a few selected cases, which are shown in Fig. 9. Five cases are displayed, and between subsequent cases a single parameter of the MVG was changed to visualise the difference. The first case is close to the base configuration C02 of the experiments of Sattarzadeh and Fransson [22] ($\hat{d}/\hat{\Lambda} = 0.2$, $\Lambda = 13.5$ mm, $h = 1.3$ mm). Between Cases (1)–(2), $\hat{d}/\hat{\Lambda}$ was increased to 0.5. Then, in Case (3), the spanwise periodicity $\hat{\Lambda}$ is enlarged to 26.5 mm. In Case (4), heightened MVGs are investigated with $\hat{h} = 1.9$ mm. Finally, in Case (5), once again, $\hat{d}/\hat{\Lambda}$ is changed, in this case to 0.35. The parameter values for each case can be found in the caption of Fig. 9. The left and right upper figures display the integral- and difference-based streak amplitude evolution, respectively. The evolution of the streamwise vorticity $\Omega_x$ of the base flow is also analysed to learn more about the generation of streaks through the lift-up mechanism. $\Omega_x$ is plotted in streamwise cross sections; rows 2–6 in Fig. 9 display cases (1)–(5), and each column corresponds to a streamwise location, displayed with the dashed vertical lines in the two upper figures. Note that the spanwise extent of the streamwise vorticity plots of Cases (1) and (2) is larger than the actual periodicity $\hat{\Lambda}$.

First, the effect of increasing $\hat{d}/\hat{\Lambda}$ from 0.2 to 0.5 is analysed. Comparing the streak amplitudes (blue and red curves), remarkably different behaviour can be observed for the two amplitude definitions. Although both amplitude measures show that in the downstream region Case (2) is higher than Case (1), near the maximum amplitude the trends are different. The maximum value of $A_{\mathrm{ST}}^{\mathrm{int}}$ is twice as high in Case (2) than in Case (1), and Case (2) is always higher than Case (1). However, looking at $A_{\mathrm{ST}}^{\mathrm{diff}}$ the maximum of Case (2) is lower than the maximum of Case (1). Turning our attention to the streamwise vortex evolution, the following thoughts can be recorded.

In Case (1), because of the close spacing, the vortices start to interact immediately, which results in a strong streak generation, but also a fast depletion of $\Omega_x$. In Case (2), due to the larger spacing, the slower interaction of the vortices results in a less intensive but more sustained streak generation. This is apparent in the third column, since the streamwise vorticity is stronger in Case (2) than in Case (1). These observations regarding $\Omega_x$ align with the behaviour displayed by $A_{\mathrm{ST}}^{\mathrm{diff}}$, but not reflected in the case of $A_{\mathrm{ST}}^{\mathrm{int}}$. $A_{\mathrm{ST}}^{\mathrm{int}}$ was introduced by Shahinfar et al. [17] to measure the modulation of the flow in the cross section; therefore, moving the vortices apart in Case (2) increases the streak amplitude compared to Case (1) since the streaks occupy a larger cross-section of the flow. This suggests that $A_{\mathrm{ST}}^{\mathrm{diff}}$ can capture the qualitative differences of the streaky boundary layer better than $A_{\mathrm{ST}}^{\mathrm{int}}$.

Next, Cases (2) and (3) are compared (red and yellow lines, rows 3 and 4), where the impact of changing the spanwise extent of the computational domain is visible. It is apparent from the figures displaying the streamwise vorticity that an increase in $\hat{\Lambda}$ separates the vortices, which enables them to grow as they evolve downstream. The slower vortex interaction results in a slower but more persistent streak evolution, which is reflected by both streak amplitudes: Case (3) has a lower maximum than Case (2), but the amplitude substantially higher downstream. Note that in the case of $A_{\mathrm{ST}}^{\mathrm{int}}$, the maximum amplitude of Case (3) is smaller by a factor of two than Case (2). This is because the vortices occupy a smaller portion of cross-section due to the increase in $\hat{\Lambda}$.

Comparing Cases (3) and (4) (yellow and purple line, rows 4 and 5) the influence of changing $\hat{h}$ can be analysed. An increased MVG

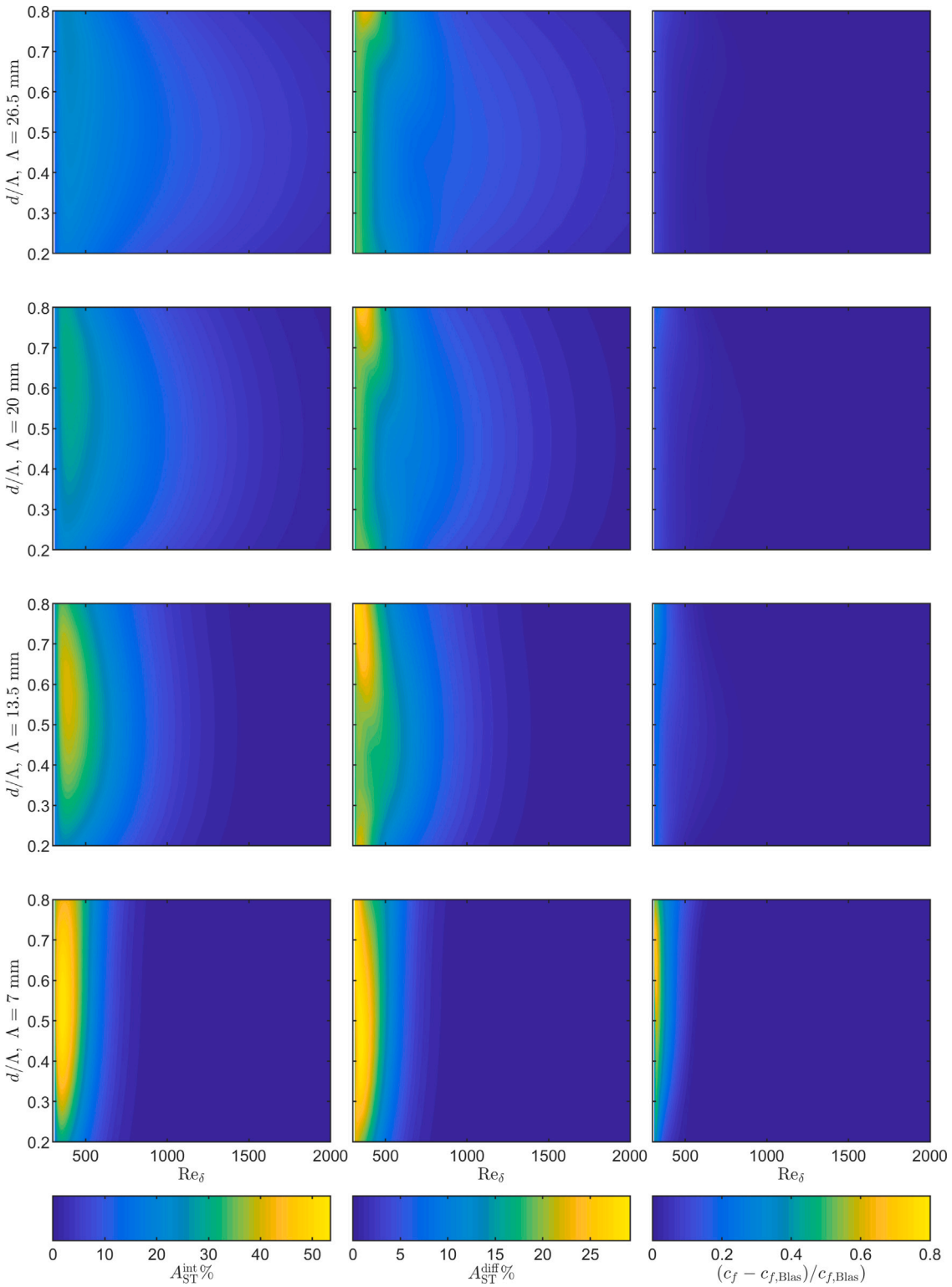


**Fig. 7.** Streak amplitude evolution as a function of Re and $\hat{d}/\hat{\Lambda}$ in the parametric study, $h = 1.3$ mm. The first, second and third columns display the $A_{\mathrm{ST}}^{\mathrm{int}}$, $A_{\mathrm{ST}}^{\mathrm{diff}}$ and the relative difference in the spanwise averaged skin friction coefficient w.r.t to the Blasius boundary layer, respectively. Each row displays the result for a different value of $\Lambda$.

height results in a stronger streamwise vorticity generation, as apparent from row 5. Because of the very strong concentration of the initially generated streamwise vorticity, the growth of the vortices is more pronounced than in Case (3). Turning our attention to the streak amplitudes, $A_{\mathrm{ST}}^{\mathrm{int}}$ once again has a monotonic increase followed by a monotonic decrease. Increasing $\hat{h}$ also results in an increase in the maximum of $A_{\mathrm{ST}}^{\mathrm{int}}$ by more than a factor of two. On the other hand, the relative difference in the maximum of $A_{\mathrm{ST}}^{\mathrm{diff}}$ is much lower, around 36%. Furthermore, qualitative differences can be found in $A_{\mathrm{ST}}^{\mathrm{diff}}$ compared to $A_{\mathrm{ST}}^{\mathrm{int}}$: $A_{\mathrm{ST}}^{\mathrm{diff}}$ has a plateau around $\mathrm{Re}_\delta \in [700, 900]$. This may be attributed to the following: first, in the aft of the MVGs, vortices start the generation of streaks. Then, as the counter-rotating vortices grow downstream, they start a renewed constructive interaction (see the third column, corresponding to $\mathrm{Re}_\delta = 700$), resulting in an increased

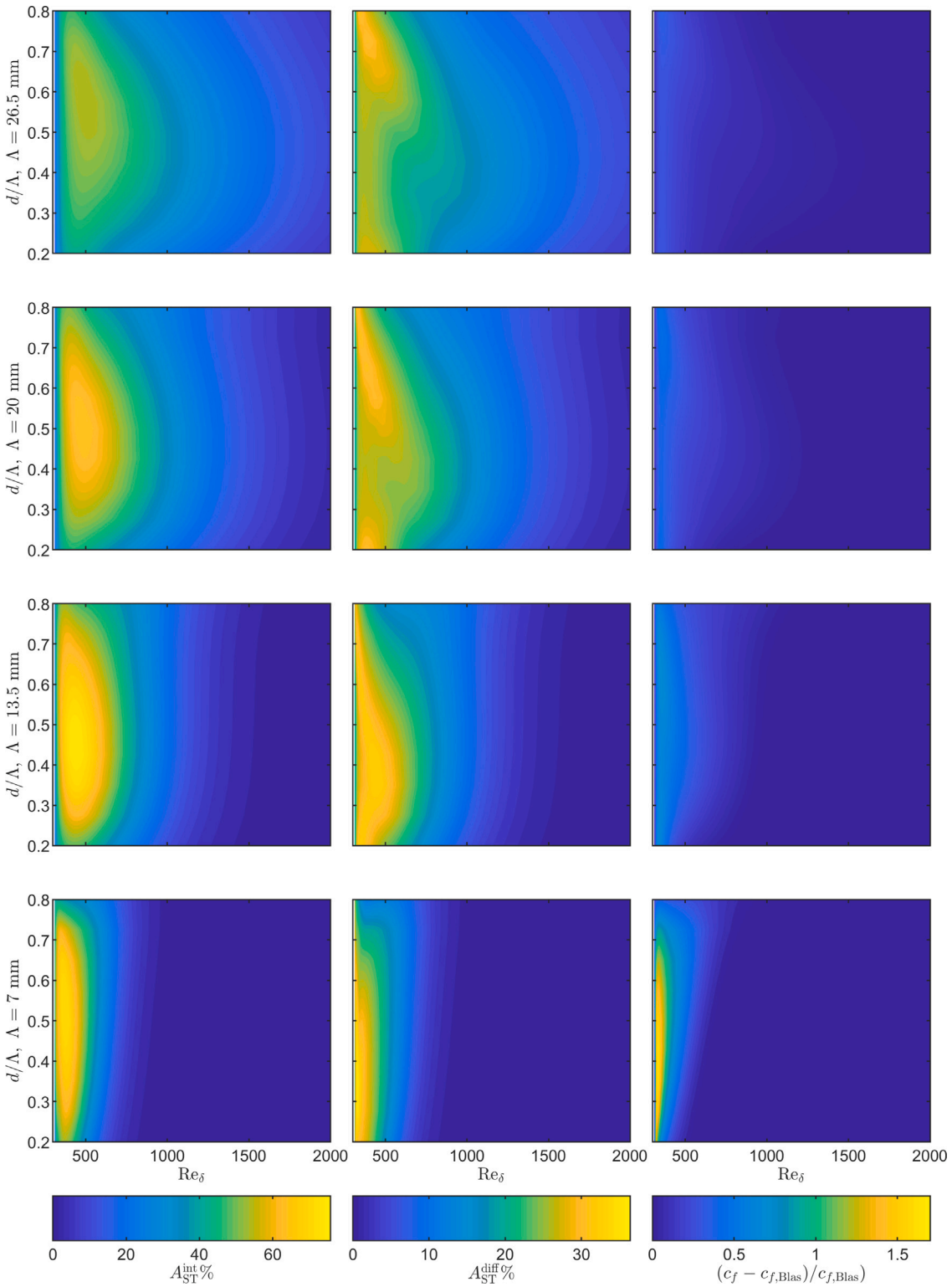


**Fig. 8.** Streak amplitude evolution as a function of Re and $\hat{d}/\hat{\Lambda}$ in the parametric study, $h = 1.9$ mm. The first, second and third columns display the $A_{\mathrm{ST}}^{\mathrm{int}}$, $A_{\mathrm{ST}}^{\mathrm{diff}}$ and the relative difference in the spanwise averaged skin friction coefficient w.r.t to the Blasius boundary layer, respectively. Each row displays the result for a different value of $\Lambda$.

streak generation. Therefore, once again, $A_{\mathrm{ST}}^{\mathrm{diff}}$ seems to describe better the qualitative changes in the base flow than $A_{\mathrm{ST}}^{\mathrm{int}}$.

Concluding the discussion of the streamwise vorticity, it is noted that the although in Case (4) the spacing of the MVGs is equidistant, the spacing of the vortices generated by them is not. This is because the MVG location is defined at its centre, while the vortices are generated at the aft of the MVGs. To create equidistant vortices, in Case (5), $\hat{d}/\hat{\Lambda}$ is decreased to 0.35. As it can be seen in row (6), the vortices are indeed spaced more equally than in Case (4). Looking at the streak amplitudes, no significant difference can be observed. Interestingly, some changes can be observed in the case of $A_{\mathrm{ST}}^{\mathrm{diff}}$: once again, a plateau can be observed, but the it appears further downstream than in Case (4). The qualitative changes are likely to be connected with the interaction of the vortices.

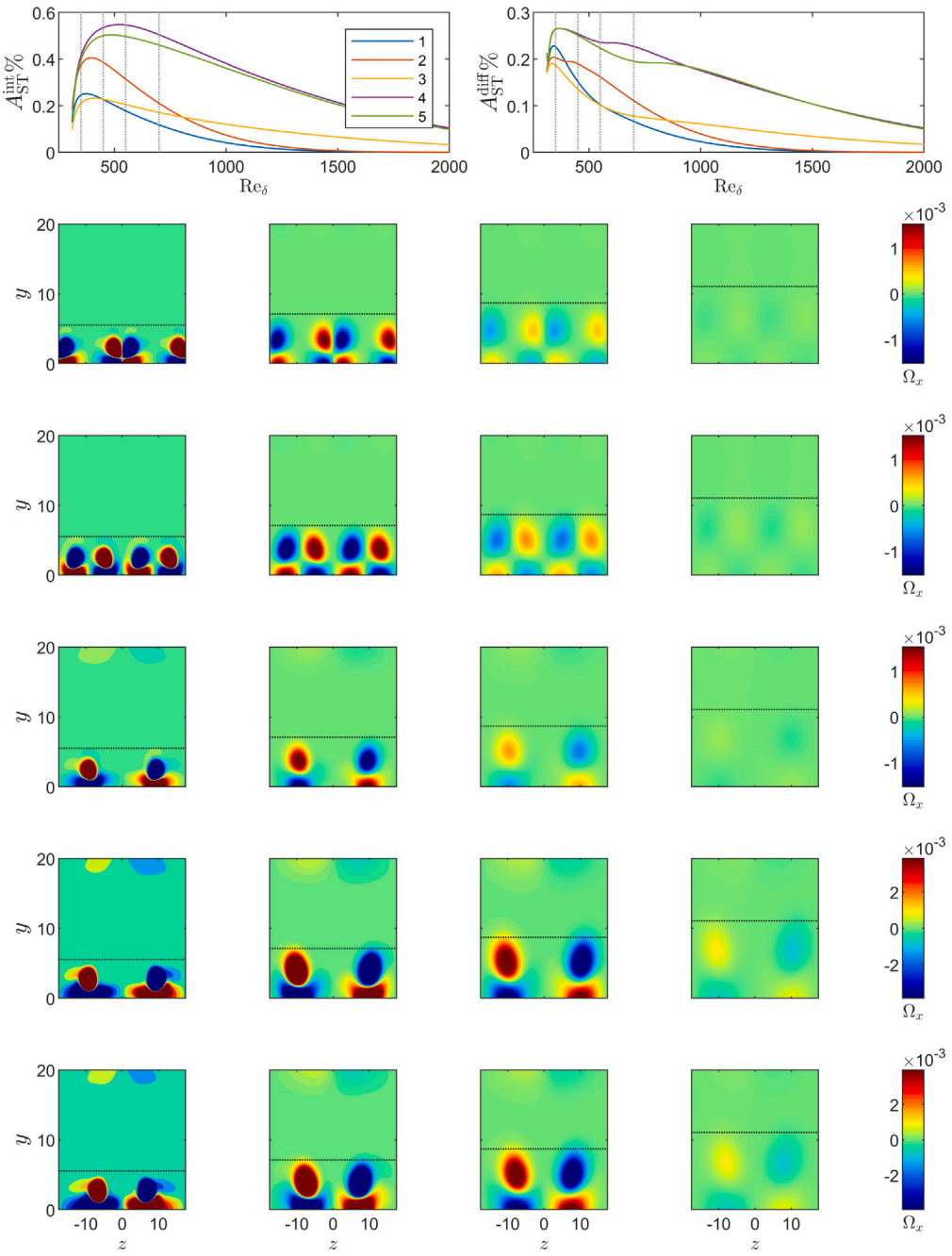


**Fig. 9.** A collection of figures offering more insight into the streaky boundary layer evolution. The left and right figures in the first row present the integral and difference based streak amplitude, respectively. In rows 2–6, the streamwise vorticity $\Omega_x$ is displayed for cases (1)–(5) at four different streamwise locations in successive order ($Re_\delta$ = 450, 550, 700, and 1000), which are shown in the top figures with dashed vertical lines. In the figures of the streamwise vorticity, the horizontal lines denote the boundary layer edge $\delta_{99}$ of the Blasius boundary layer at the corresponding location. The parameters of the five cases are the following. (1): $\hat{d}/\hat{\Lambda} = 0.2$, $\hat{\Lambda} = 13.5$ mm, $\hat{h} = 1.3$ mm. (2): $\hat{d}/\hat{\Lambda} = 0.5$, $\hat{\Lambda} = 13.5$ mm, $\hat{h} = 1.3$ mm. (3): $\hat{d}/\hat{\Lambda} = 0.5$, $\hat{\Lambda} = 26.5$ mm, $\hat{h} = 1.3$ mm. (4): $\hat{d}/\hat{\Lambda} = 0.5$, $\hat{\Lambda} = 26.5$ mm, $\hat{h} = 1.9$ mm. (5): $\hat{d}/\hat{\Lambda} = 0.35$, $\hat{\Lambda} = 26.5$ mm, $\hat{h} = 1.9$ mm.

The careful reader may wonder about the vorticity at $y \approx 20$ in the first columns of Fig. 9. These vorticity spots appear because of the vortices generated by the MVGs, as they induce a fast downstream jet around $z = 0$, which extends into the free stream. Note that the colour limits are chosen so that small vorticity values are visible at downstream locations: the vorticity generated by the MVGs is $\approx 100$ times higher than the outer vorticity. Furthermore, the low order finite element and the large elements used in the far field (see Fig. 2(b)) may cause numerical inaccuracies that magnify the outer vorticity values. It was checked that refining the grid in the far-field does not influence the results. Therefore, the outer vorticity is not considered significant.

Next, the right column of Fig. 7 displaying the relative difference in the local skin friction compared to the Blasius boundary layer is examined for $\hat{h} = 1.3$ mm. In all cases, the differences are quite low, which suggests that the additional induced drag of the MVGs is very small compared to the potential gain due to transition delay. This aligns with the experimental observations of Shahinfar et al. [17]. For low values of $\hat{\Lambda}$, large differences can be observed upstream; as $\hat{\Lambda}$ is increased, notable differences only remain for high values of $\hat{d}/\hat{\Lambda}$. This, once again, shows that MVGs with $\hat{d}/\hat{\Lambda} \approx 0.5$ are advantageous compared to previous ones with $\hat{d}/\hat{\Lambda} \approx 0.2$. The same trends can be deduced from the last column of Fig. 8 for $\hat{h} = 1.9$ mm, which further supports our previous observations. A more quantitative analysis of the

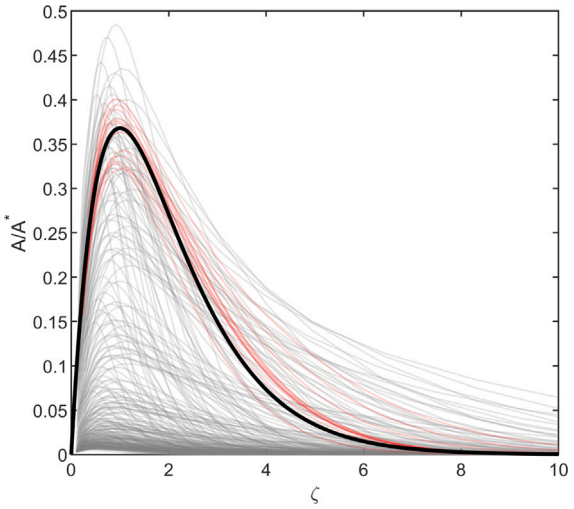


**Fig. 10.** Scaled streak amplitudes using the formula of Sattarzadeh and Fransson [22]. The solid black line denotes the amplitude curve into which the simulated (shaded grey) amplitude curves are supposed to collapse. The shaded red curves denote the simulation of the experiments of Sattarzadeh and Fransson [22], which are the rescaled versions of the curves displayed in Fig. 4.

drag reduction, that also incorporates the transition prediction, will be presented in the next section.

As a concluding investigation, we compare the integral streak amplitude evolution with the scaling proposed by Sattarzadeh and Fransson [22] (an extension of the previous work of Shahinfar et al. [17]). They proposed a nondimensionalisation that depends on the geometric parameters of the MVGs, that collapsed the individual streak amplitude curves into a single one. For the details of the nondimensionalisation the reader is referred to Sattarzadeh and Fransson [22]. The nondimensional streak amplitude $A/A^*$ is displayed as a function of the nondimensional streamwise coordinate $\zeta$ in Fig. 10. The thick black line denotes the amplitude curve the different cases supposed to collapse into. The faint red lines denote the simulations of the experiments of Sattarzadeh and Fransson [22], which indeed follow the black line very closely. However, some of the experimental curves diverge significantly from the proposed scaling far downstream. The cases of the parametric study that are displayed with the grey lines, deviate significantly from the proposed scaling. This shows that unfortunately, the scaling proposed by Sattarzadeh and Fransson [22] has only a limited range of validity. Even if the streak amplitude were be scaled using the actual maximum value $A^*$ instead of the fitted one, and not by the scaling proposed by Sattarzadeh and Fransson [22], the streak evolution prediction would be poor. Therefore, establishing a functional relationship between the streak amplitude evolution and the geometric parameters of the MVG is not attempted.

### 3.3. Parametric study: stability of the streaky boundary layer

This section discusses the results of the stability calculation in the case of the parametric study. The parameter set is described in the beginning of Section 3. First, the results of the secondary broadband stability calculations are presented. In this, we illustrate the challenging aspect of separating the unstable modes; then, we evaluate and compare both $N$ and $N_{\mathrm{MU}}$ as a measure of the secondary instability. After this, the transition Reynolds number calculated with the conservative value of $N = 7$ is discussed. This is followed by identifying the optimum MVG configurations of the parametric study w.r.t. to the investigated parameters. Next, an estimate for the possible drag reduction is presented. Finally, recommendations are given for choosing the MVG parameters, based on the results of the simulations.

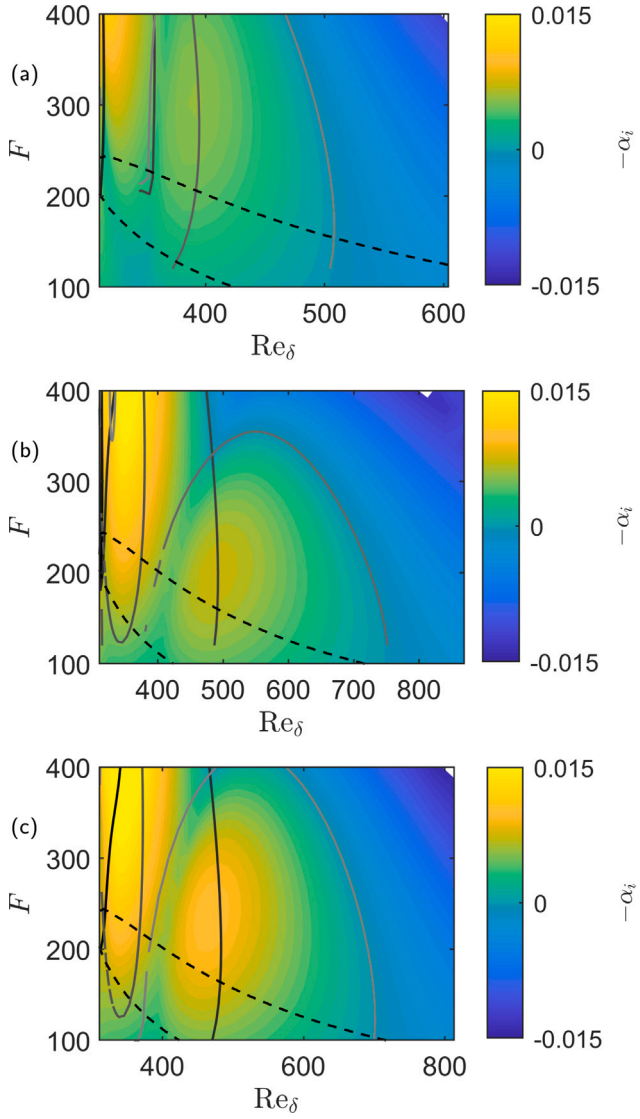


**Fig. 11.** Most unstable growth-rate of the secondary instabilities as a function of Re and $F$, indicating the emergence of secondary instabilities. The solid lines display the neutral curves of the individual unstable modes, and the dashed line displays the neutral curve of the undisturbed Blasius boundary layer. Compared to the base case (a), secondary instabilities develop due to the increase in $\hat{d}/\hat{\Lambda}$ (b), or decrease in $\Lambda$ (c). The parameters are the following: (a): $\hat{h} = 1.7$ mm, $\hat{d}/\hat{\Lambda} = 0.5$, $\hat{\Lambda} = 26.3$ mm; (b) $\hat{h} = 1.7$ mm, $\hat{d}/\hat{\Lambda} = 0.65$, $\hat{\Lambda} = 26.3$ mm; (c)): $\hat{h} = 1.7$ mm, $\hat{d}/\hat{\Lambda} = 0.5$, $\hat{\Lambda} = 16.75$ mm.

In Fig. 11, the secondary instability maps are presented for three different cases. Here, similarly to Fig. 5(b), the growth rate of the most unstable eigenmode is displayed, the continuous lines denote the neutral curves of the individual modes, and the dashed line displays the neutral curve of the TS waves in the undisturbed Blasius boundary layer. In Fig. 11(a), the parameters of the MVG are $\hat{d}/\hat{\Lambda} = 0.5$, $\hat{\Lambda} = 26.5$ mm and $\hat{h} = 1.7$ mm. Starting from this configuration, a single parameter is changed in the two other cases: in Figs. 11(b) and 11(c), the altered parameters are $\hat{\Lambda} = 23.35$ mm and $\hat{d}/\hat{\Lambda} = 0.65$, respectively.

In the reference configuration, four unstable modes can be distinguished. This case illustrates well the problem of the unstable mode separation, that is highlighted by the discontinuity of the neutral curves of the individual modes. Despite the incomplete neutral curves, the maximum $N$ value could be clearly identified in each case. This case can be considered relatively stable: the highest $N$ factor arises from the mode with the largest streamwise extent, giving a value of $N = 1.5$. In the other two cases displayed in Figs. 11(b) and 11(c), lowering

$\hat{\Lambda}$ and increasing $\hat{d}/\hat{\Lambda}$ destabilises the boundary layer, and a new secondary instability arises. This corresponds to the sinuous secondary eigenmode that was found by Andersson et al. [11] and Martín and Paredes [27,28]; which was verified by examining the eigenfunctions (not shown).

The secondary sinuous eigenmode is unstable on a much larger streamwise interval than the rest of the modes; note the different $x$ axis limits of the subfigures, and also the correspondence between the modes. In the calculation of the $N$ factor, large values can be attributed to this unstable mode. This shows that strong destabilisation, *within the present modelling framework that does not consider the flow field very close to the MVG*, is related to emergence of sinuous secondary instabilities, different than those displayed in Fig. 11(a) that are related to the near-wake flow of the MVG. The reason why the proposed $N_{\mathrm{MU}}$ factor gives a reliable estimate of the $N$ factor can also be explained by this: the near-wake modes have a small contribution to the $N$ factor, compared to the new secondary modes that dominate the destabilisation. Therefore, the estimate also captures the dominant destabilisation, while it discards the near-MVG wake modes that are hard to distinguish from each other and have little contribution to the simplified $N$ factor calculation.

It must be noted that because of the finite frequency interval covered in the secondary stability calculation, the actual maximum $N$ factor may lie outside the investigated frequency range. Despite this, if strong secondary destabilisation is observed, it also results in high $N$ values within the investigated frequency interval. Therefore, the frequency range used in this study is sufficient to indicate cases with strong destabilisation that should be avoided.

The results of the secondary instability calculation are displayed in Fig. 12 as function of $\hat{\Lambda}$ and $\hat{d}/\hat{\Lambda}$. The first and second columns display $N$ and $N_{\mathrm{MU}}$, respectively. The three rows show the values for $\hat{h} = 1.3$, 1.5 and 1.7 mm, respectively. The colours show the magnitude of the $N$ factor, but the numerical values are also displayed. Both measures of destabilisation yield both qualitatively and quantitatively the same results, which supports that $N_{\mathrm{MU}}$ can be used as a reliable tool to assess the secondary instability of MVGs.

Low values of $\hat{\Lambda}$ and high values of $\hat{d}/\hat{\Lambda}$ are responsible for strong secondary instability, and these regions should be avoided so that transition is not advanced. Interestingly, the highest secondary instability does not arise at the combination of low $\hat{\Lambda}$ - high $\hat{d}/\hat{\Lambda}$; however, this was not investigated in detail. The strong secondary instability is likely because both effects generate a very strong shear layer that leads to a rapid boundary layer modification - these effects can be observed in Figs. 7 and 8 using either of the two amplitude measures. Furthermore, it can also be observed that the region of lowest instability is for high $\hat{\Lambda}$ and low $\hat{d}/\hat{\Lambda}$. As the MVG height is increased, the region of strong secondary instability expands in the $\hat{\Lambda}$- $\hat{d}/\hat{\Lambda}$ plane, but the high $\hat{\Lambda}$ - low $\hat{d}/\hat{\Lambda}$ region remains safe with respect to the secondary instability.

For the highest MVG, only $N_{\mathrm{MU}}$ was calculated, since separation of the individual eigenmodes was not possible using the current streamwise resolution in the BiGlobal stability calculations. This is shown in Fig. 13. No qualitative change can be observed to the case of $\hat{h} = 1.7$ mm (Figs. 12(e) and 12(f)). Low values of $\hat{d}/\hat{\Lambda}$ do not promote secondary instability; and for a large spanwise periodicity $\hat{\Lambda}$, increasing $\hat{d}/\hat{\Lambda}$ is not possible without the generation of strong secondary instabilities. These results once again demonstrate the effectiveness of the proposed $N_{\mathrm{MU}}$ factor.

Next, the attenuation of the TS waves is investigated in the downstream portion of the boundary layer, which is examined through the transition Reynolds number calculated with the conservative $N = 7$ value. The data are plotted as a function of $\hat{\Lambda}$ and $\hat{d}/\hat{\Lambda}$ in Fig. 14, where each subfigure corresponds to a different MVG height. The colours show the transition Reynolds number, and the numbers display the increment compared to the Blasius boundary layer, calculated using the Orr–Sommerfeld equation.

In the case of $\hat{h} = 1.3$ mm, a clear maximum can be found at $\hat{\Lambda} = 16.75-20$ mm and $\hat{d}/\hat{\Lambda} = 0.5$. that achieves a moderate 100 increase in the critical Reynolds number. Note that $\hat{d}/\hat{\Lambda} = 0.5$ corresponds to the spacing suggested by studies using optimal vortices. As $\hat{h}$ is increased to 1.5 mm, the increment in the transition Reynolds number is almost doubled compared to the previous MVG height, while the optimum is achieved for the same $\hat{d}/\hat{\Lambda}$ but for a higher value of $\hat{\Lambda}$. Increasing the MVG height further results in a continued improvement in the transition delay. However, for cases $\hat{h} = 1.7$ and 1.9 mm, no definite maximum can be observed within the investigated parameter interval. For $\hat{d}/\hat{\Lambda} = 0.5$, where which the maximum value was found in each height, the transition delay monotonically increases with higher values of $\hat{\Lambda}$. Interestingly, a strong stabilisation can also be observed for $\hat{d}/\hat{\Lambda} = 0.35$, especially in the case of $\hat{h} = 1.9$ mm. This suggests that as the MVG height is increased, the strongest attenuation of TS waves moves away from $\hat{d}/\hat{\Lambda} = 0.5$ towards lower values of $\hat{d}/\hat{\Lambda}$. Note that as reported by Martín and Paredes [27] and as also observed in Fig. 4(c), the BRE predict a slower streak decay compared to DNS or experiments, meaning that in real applications a slightly deteriorated transition delay may be observed.

For a more exhaustive evaluation, all the cases are plotted in the $\mathrm{Re}_{\mathrm{Tr}}$ - secondary instability $N$ factor plane, which is shown in Fig. 15. The top and bottom figures display $N$ and $N_{\mathrm{MU}}$ on the $y$ axis, respectively. The black line shows the convex hull of all the cases, and the lower-right portion of the curve can be considered as the Pareto front of the cases. As a reference, the calculations of the experiments of Sattarzadeh and Fransson [22] are also plotted.

The difference between the two $N$ factors is manifested as a vertical shift of the points. Both for $\hat{h} = 1.7$ and 1.9 mm, favourable cases were found in the parametric study compared to the experimental ones w.r.t to the investigated metrics. The best experimental case can be considered the rightmost one (for which the free-stream velocity is 8.5 m/s), since this yields the best transition delay, and the experimentalists did not report breakdown to turbulence due to either secondary convective or absolute instability. Cases with $\hat{\Lambda} = 26.5$ mm and both $\hat{d}/\hat{\Lambda} = 0.35$ and 0.5 display better transition delay properties for MVG heights $\hat{h} = 1.7$ and 1.9 mm than the best experimental setup. Note, however, that the optimum transition delay w.r.t. $\hat{\Lambda}$ and $\hat{d}/\hat{\Lambda}$ was not found in the case of $\hat{h} = 1.7$ and 1.9 mm; therefore, even better transition delay may be achieved.

Next, the force gain is evaluated in the present calculation for quantitative assessment of the drag reduction of the best cases. The spanwise averaged force and relative force difference is calculated to assess the effectiveness of the MVG:

$$F_{\mathrm{Blasius}} = \int_{x_0}^{x_{Tr,\mathrm{Blasius}}} c_{f,\mathrm{Blasius}}(x)\mathrm{d}x + \int_{x_{Tr,\mathrm{Blasius}}}^{x_{Tr}} c_{f,\mathrm{Turb}}(x)\mathrm{d}x, \tag{18}$$

$$F_{\mathrm{MVG}} = F_{\mathrm{MVG,CFD}} + \int_{x_{1,\mathrm{CFD}}}^{x_{Tr}} c_{f,\mathrm{BRE}}(x)\mathrm{d}x. \tag{19}$$

The spanwise averaged force is calculated between $x_0$, the start of the three-dimensional CFD calculation, and the transition location $x_{Tr}$ in the streaky boundary layer. In the case of the reference Blasius boundary layer, the force can be calculated from two contributions: the reference Blasius boundary layer ($c_{f,\mathrm{Blasius}}$), and the part where the boundary layer would become turbulent without the MVGs ($c_{f,\mathrm{Turb}}$). In the Blasius boundary layer, the transition location $x_{Tr,\mathrm{Blasius}}$ was calculated from the solution of the Orr–Sommerfeld equation. In the turbulent portion, the skin friction coefficient was calculated using the formula $c_{f,\mathrm{Turb}} = 0.0592 \cdot \mathrm{Re}_x^{-1/5}$, similarly to Shahinfar et al. [17]. The spanwise mean force of the modified boundary layer is also calculated in two parts. The force acting on (and near) the MVGs is obtained from the three-dimensional CFD calculations. Then, the spanwise averaged skin friction coefficient, obtained from the solution of the BRE, is integrated between the downstream end of the CFD calculation domain (see Fig. 1(a) and Table 1) and the transition location in the modified $x_{Tr}$. For MVG height 1.9 mm, the relative force difference ($F_{\mathrm{Blasius}}$ −

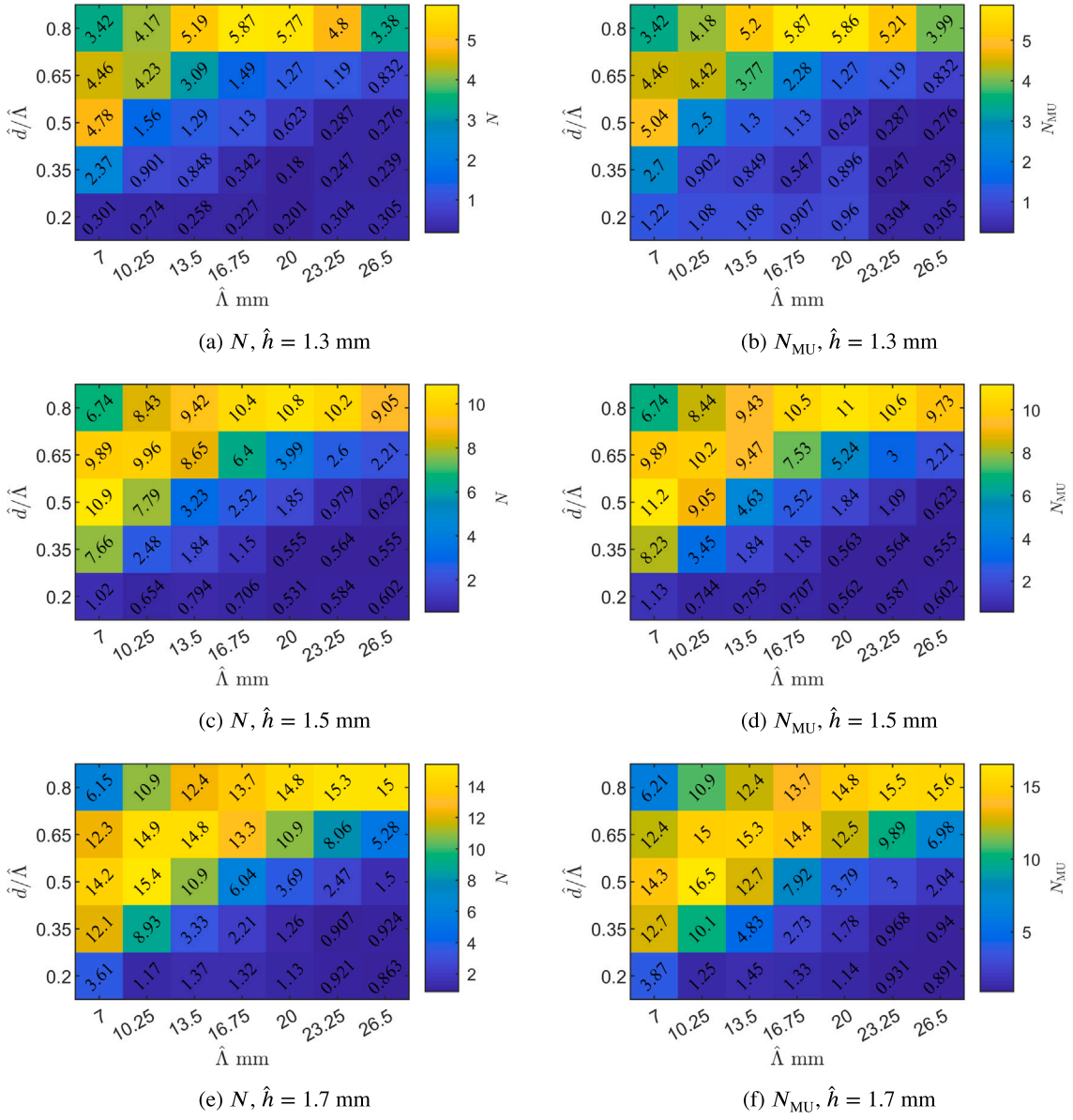


(a) $N$, $\hat{h} = 1.3$ mm (b) $N_{MU}$, $\hat{h} = 1.3$ mm

(c) $N$, $\hat{h} = 1.5$ mm (d) $N_{MU}$, $\hat{h} = 1.5$ mm

(e) $N$, $\hat{h} = 1.7$ mm (f) $N_{MU}$, $\hat{h} = 1.7$ mm

**Fig. 12.** Maximum $N$ factor of the near field secondary instabilities as a function of $\hat{\Lambda}$ and $\hat{d}/\hat{\Lambda}$. The first, second and third row displays $\hat{h} = 1.3$, 1.5 and 1.7 mm, respectively; the first and second column displays $N$ and $N_{MU}$, respectively.

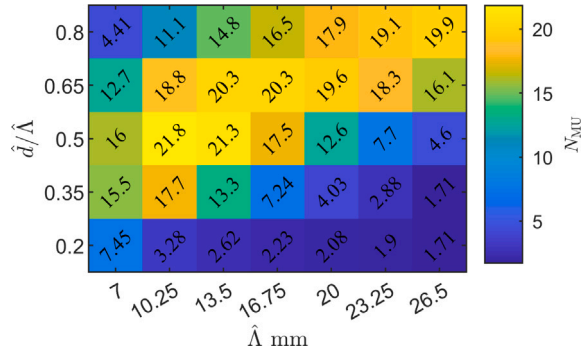


**Fig. 13.** Maximum $N$ factor of the near field secondary instabilities as function of $\hat{\Lambda}$ and $\hat{d}/\hat{\Lambda}$, calculated with the maximum growth rate from the eigenspectrum. $\hat{h} = 1.9$ mm.

$F_{MVG})/F_{Blasius}$ is plotted in Fig. 16. For the optimum cases within the parametric study, a 60% drag reduction is reported. Despite the relative small increase in the streamwise extent of the laminar flow region, a significant drag reduction is predicted from the calculations.

Using the results of the stability calculations and the streak amplitude evolutions, some recommendations are made for the choice of the MVG parameters. For this, a nondimensional MVG height $h = \hat{h}/\hat{\delta}_{99}(x = x_{MVG})$ and $\hat{\Lambda}/\hat{h}$ is used. For $\hat{h} = [1.3, 1.5, 1.7, 1.9]$ mm, the values of $h$ are $[0.3601, 0.4155, 0.4709, 0.5263]$.

- For $h < 0.45$, $\hat{d}/\hat{\Lambda} = 0.5$ is the clear optimum for the spacing within MVG pairs, considering both attenuation of the TS waves and secondary instability. Above $h = 0.45$, $d/\Lambda$ should be decreased to avoid secondary instabilities.
- If the optimum is taken for MVG heights 1.3, 1.5 and 1.7 mm at $\hat{\Lambda} = 20$, 23.25 and 26.5 mm (for $\hat{d}/\hat{\Lambda} = 0.5$), this gives $\hat{\Lambda}/\hat{h}$ 15.38, 15.50 15.59, respectively. Therefore, $\hat{\Lambda}/\hat{h} \approx 15$ seems a reasonable choice for the spanwise periodicity of the MVG pairs.

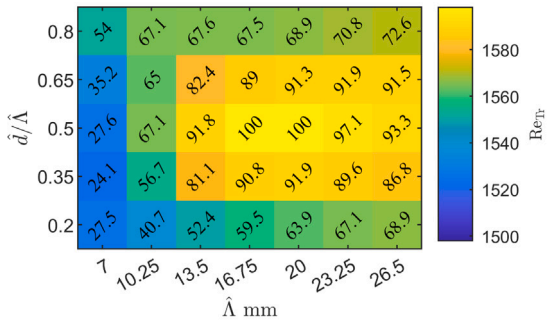


(a) $\hat{h} = 1.3$ mm

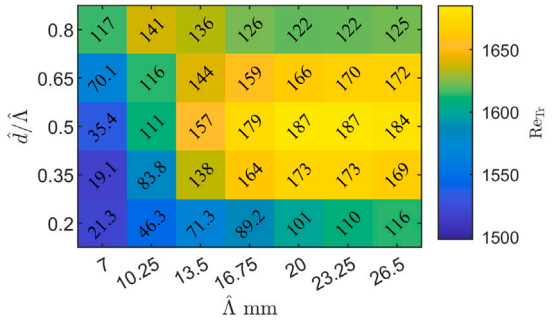


(b) $\hat{h} = 1.5$ mm

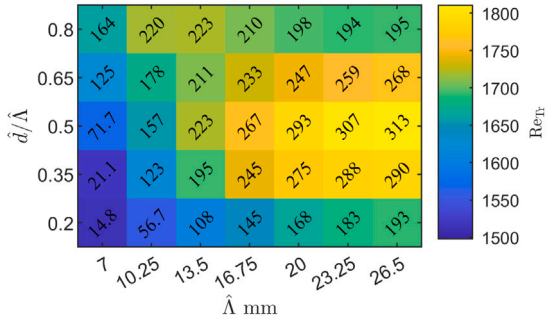


(c) $\hat{h} = 1.7$ mm

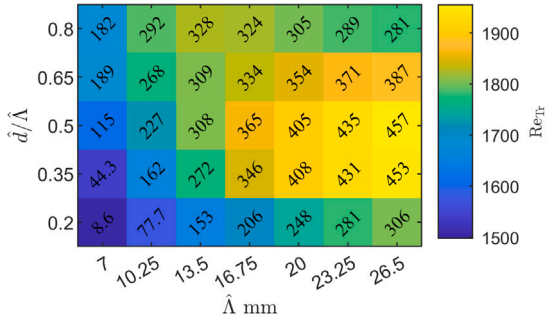


(d) $\hat{h} = 1.9$ mm

**Fig. 14.** Transition Reynolds number as a function of $\hat{\Lambda}$ and $\hat{d}/\hat{\Lambda}$, calculated for the TS waves for $N = 7$. The colour displays the transition Reynolds number, while the numbers show the increment compared to the transition location of the Blasius boundary layer (Orr–Sommerfeld solution).

Note that these values are significantly different from those used in previous experimental studies that utilised $\hat{d}/\hat{\Lambda} = 0.22$ and $\hat{\Lambda}/\hat{h} = 10.47$ [22,23], suggesting that the previously used MVG geometries could be substantially improved. It is stressed that because of the strong limitations of local linear stability theory, these recommendations should be verified in wind tunnel experiments or high fidelity DNS.

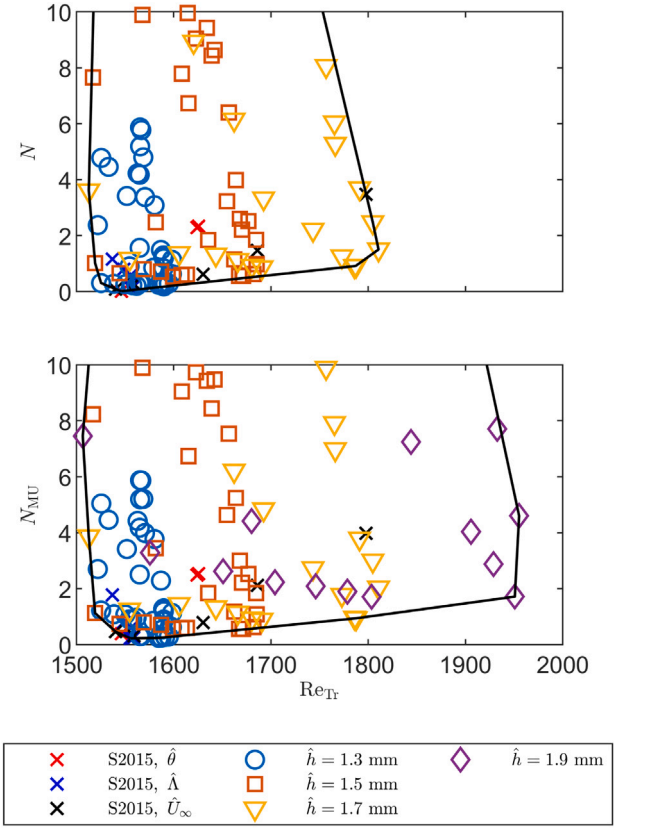


**Fig. 15.** The different cases plotted in the $\mathrm{Re}_{Tr}$ - secondary instability $N$ plane. The upper figure displays the maximum mode $N$ factor, and the lower figure displays the $N$ factor calculated with the most unstable eigenmode of the spectrum. The black line displays the convex hull of the cases; the lower-right portion of the convex hull can be considered the Pareto front of the eigenvalues.

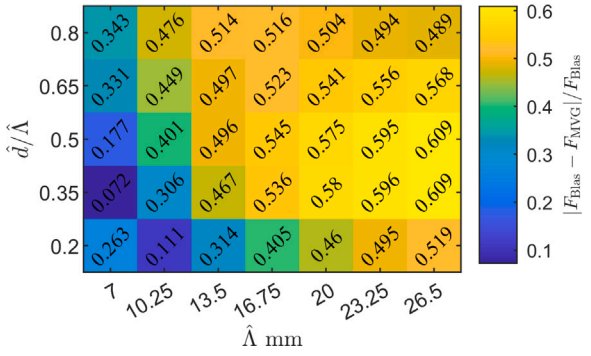


**Fig. 16.** Relative force decrease between the MVG and the Blasius boundary layer as a function of $\hat{\Lambda}$ and $\hat{d}/\hat{\Lambda}$, $h = 1.9$ mm. The spanwise mean skin friction coefficient is integrated between the start of the computational domain (CFD) and the transition location of the MVGs.

### 3.4. Additional aspects

Before concluding the analysis, some additional aspects of the MVGs are discussed. These are non-local effects, which are analysed using

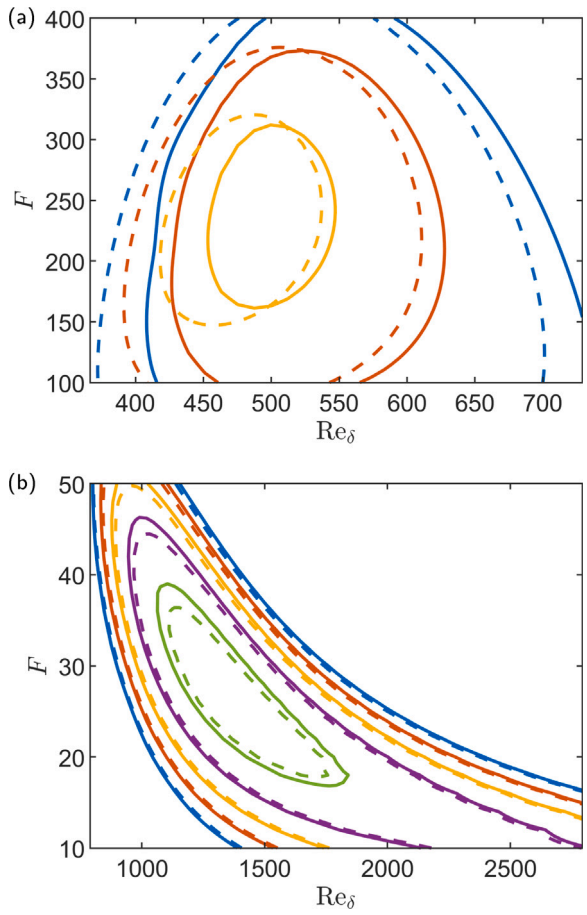


**Fig. 17.** Comparison of the growth rate contours of the BiGlobal (dashed) and PSE (solid) in the Re – $F$ plane. a: secondary sinuous mode; the contour correspond to $\mu = [0, 4, 8] \cdot 10^{-3}$. b: TS waves; the contour correspond to $\mu = [-4, 0, 4, 8, 10] \cdot 10^{-4}$. The MVG parameters are the following: $\hat{h} = 1.7$ mm, $\hat{d}/\hat{\Lambda} = 0.5$, $\hat{\Lambda} = 16.75$ mm (same as Fig. 11(c)).

plane-marching PSE for a single MVG configuration. Then, absolute instability, and roughness-induced transition are covered briefly.

Fig. 17 shows the growth rate contours for the secondary sinuous mode (Fig. 17(a)) and the TS waves (Fig. 17(b)). The dashed lines are the results of the BiGlobal stability calculation, the solid lines display the PSE solution. The parameters of the MVG are $\hat{h} = 1.7$ mm, $\hat{d}/\hat{\Lambda} = 0.5$, and $\hat{\Lambda} = 16.75$ mm. This configuration is the same as displayed in Fig. 11(c); the choice was motivated by the fact that this configuration exhibits both strong stabilisation of the TS waves but also significant secondary instability. It stands out from both figures that non-local effects play an important role. The discrepancy between the two methods is more significant in the case of the secondary instability, which is located more upstream, where non-parallel effects are more substantial. The comparison highlights the importance of non-local effects; however, since no qualitative differences can be found, our approach – large number of BiGlobal stability computations to restrict the parameter space, then switching to PSE – is not refuted.

Next, the question of absolute instability is discussed briefly. As mentioned in Section 2.2, the calculation of the three-dimensional base flow cannot capture absolute instability because of the (i) stationary form of the NS equations is solved, and (ii) only half of the geometry is simulated with symmetry boundary condition. However, in the case of the MVG with nearly the best parameters ($\hat{h} = 1.9$ mm, $\hat{d}/\hat{\Lambda} = 0.5$, $\hat{\Lambda} = 26.5$ mm), DNS of the time-dependent NS equations with the whole geometry was performed. The time step was $10^{-5}$, and 11000 time steps were simulated, for which the initial condition was the inlet velocity profile. Since the initial condition does not satisfy the governing equations, there is a transient which should be sufficient to trigger absolute instability. However, no absolute instability was found: the solution converged to a stationary value. This finding suggests that the present recommendations for the MVGs satisfy the criterion of no absolute instability; nevertheless, absolute instability may be possible for other MVG configurations, and may also be partly responsible for the discrepancy between the experimental and simulated values in the streak amplitudes.

As a final remark, an additional aspect of transition advancement due to the presence of the MVGs is discussed. It is well known that surface roughness can lead to premature transition to turbulence. The advancement of transition is known to correlate with the roughness Reynolds number $\mathrm{Re}_r = \hat{U}(\hat{y} = \hat{s})\hat{s}/\hat{\nu}$, where $\hat{s}$ is the roughness height. Recently, Weingärtner et al. [23] measured $\mathrm{Re}_r$ for their MVG configurations to assess the roughness-induced transition scenario. They found $\mathrm{Re}_r = 786$ for all of their MVGs. All the presently investigated MVGs are below this value ($\mathrm{Re}_r = 600$ for the highest MVG with $\hat{h} = 1.9$ mm). However, this does not mean that none of the MVGs investigated in the computations advance transition, since $\mathrm{Re}_r$ is expected to depend significantly on the MVG geometry and configuration. MVGs according to the proposed recommendation are spaced more sparsely than those used by Weingärtner et al. [23]; therefore, they generate a locally weaker shear layer which might result in a higher $\mathrm{Re}_r$. $\mathrm{Re}_r$ should be either calculated or measured for the proposed MVG geometries, also considering for the effect of the free-stream turbulence, which is known to significantly influence roughness-induced transition [80].

## 4. Summary and concluding remarks

In this paper, a parametric study of MVGs has been conducted to gain insight into the streak evolution, the attenuation of the TS waves and the emergence of secondary instabilities, using local linear stability analysis as a tool. Based on previous studies, the base flow was calculated using three-dimensional CFD simulations near the MVG, and the downstream evolution of the streaky boundary layer was calculated using BRE. The streaky boundary layer evolution was analysed using both the difference based and integral streak amplitudes that are common in the literature.

The stability calculations were conducted by solving the BiGlobal stability equations, with two sets of calculations for each investigated MVG case: one targeting the modified TS waves, and a second one aimed at tracking the potentially arising secondary instabilities which may advance transition. The transition location was estimated with the $e^N$ method from the TS waves using a conservative $N = 7$ value, and the $N$ factor was calculated for the secondary instabilities as an indicator as the destabilisation, since no $N$ value is available for them. Furthermore, since multiple secondary unstable modes can arise that need to be tracked separately and are hard to distinguish, as a simplification, an alternative $N_{\mathrm{MU}}$ factor was proposed. $N_{\mathrm{MU}}$ is calculated from the most unstable eigenvalue of the spectrum at each streamwise location and frequency and was found to be perfectly suitable. This substantially reduces the computational cost.

First, the experiments of Sattarzadeh and Fransson [22] were modelled. The excellent agreement of the streak amplitudes validates the base flow calculation. However, the discrepancies in some of the cases should be analysed in more detail in future studies to gain more insight for the improvement of the modelling. Although the comparison between the local stability calculations and experimental disturbance amplification values is not meaningful, the their correlation suggests that local stability analysis can give meaningful recommendations regarding the *partial* optimality of MVGs.

Examining the streak amplitude evolution, it was found that reminiscent of the optimal vortices, the spacing of the MVGs should be so that equidistant counter-rotating vortices are produced. As such, the interaction of the individual vortices can be tuned by changing the

spanwise spacing $\hat{\Lambda}$ to achieve a balance between the initial amplitude peak and far downstream persistence of the streaks. Using this we can avoid initial high streak amplitudes that can give rise to secondary instabilities, and the streak extending far downstream can successfully attenuate the TS waves. Furthermore, using the MVG height $\hat{h}$, the vortex strength can also be controlled. These findings were also supported by the analysis of the streamwise vorticity evolution: the interaction of the counter-rotating vortices determines how fast the lift-up mechanism converts the streamwise vorticity into streaks, and also affects the decay of the streaks. Furthermore, a thorough comparison of the two streak amplitude measures revealed that $A_{\mathrm{ST}}^{\mathrm{diff}}$ can better capture the qualitative changes in the flow. However, to measure the stabilisation of the flow, $A_{\mathrm{ST}}^{\mathrm{int}}$ may be more suitable as it measures the modulation of the boundary layer.

The local linear stability analysis of the streaky flow structures *suggests* that compared to the previous experimental configurations, the transition delay could be increased substantially, without significant secondary instabilities. The stability analysis unveiled similar trends as the streak amplitude analysis: $\hat{d}/\hat{\Lambda} = 0.5$ yields optimal results for a lower MVG height, which slightly decreases for increased MVG heights. These $\hat{d}/\hat{\Lambda}$ MVG spacings that produce nearly equally spaced counter-rotating vortices were not investigated before, and they show superior performance compared to previously studies on MVG spacings. Regarding the additional MVG parameters, reasonable recommendations are $\hat{\Lambda}/\hat{h} = 15$, and the calculations indicate that the MVG height can be as high as $\hat{h}/\hat{\delta}_{99} \approxeq 0.5$.

In addition to these findings, it was shown that the cumbersome tracking of the individual secondary instabilities that arise because of the very strong boundary layer modulation, can be circumvented. Using proposed $N_{MU}$ factor, calculated with the most unstable eigenmode of the spectrum, the secondary modal instabilities can be qualitatively described. This is because the strong destabilisation of the streaks is always caused by the secondary sinuous instabilities. Therefore, the $N_{MU}$ factor could be used to quantify the secondary instability of the streaky structures in future studies.

The suggestions of this study should be also investigated either experimentally, or with high fidelity direct numerical simulation. Nevertheless, the methodology of this study may be used in the optimisation of MVGs: the (relatively) efficient local linear stability calculation allow the restriction of the large parameter space of possible MVG or roughness configurations. A brief comparison of the growth rates of BiGlobal stability equations and plane marching PSE showed the importance of non-local effects; however, as no qualitative changes were observed between the two cases, the comparison support the proposed methodology. Then, additional phenomena that require more computationally intensive or more cumbersome tools can be considered.

Perhaps the best complement to this study would be stability analysis of the three-dimensional flow around, and in the close downstream vicinity of the MVGs. In the fully three-dimensional flow, global resolvent analysis is a suitable tool, which should be feasible considering the recent advancements in iterative solvers [44], randomised linear algebra [81] to find the worst-case disturbances. Furthermore, the restriction of the input space to plane wave solutions to model vorticity (gusts) and acoustic waves in the to model the excitation of the instability waves through the long–short wave conversion mechanism [41], as proposed by Kamal et al. [43], is a promising way to tackle the receptivity problem.

Finally, as pressure gradient and curvature influence the velocity profile substantially, recommendations based on the study of the Blasius boundary layer do not necessarily generalise. Although these effect should be considered in future studies, the issue of robustness, in our opinion, should be prioritised. The boundary layer is a very strongly non-normal system, which through the definition of the pseudospectrum, implies a strong sensitivity of the system (or its eigenvalues) to changes in the system [82,83]; see also Brandt et al. [84] for a discussion on the sensitivity of the lift-up and TS waves in the Blasius boundary layer. Manufacturing imperfections, or off-design operation conditions such as increased turbulence intensity, change in the free-stream velocity, increased surface roughness due to insect contamination or ice accumulation, can possibly deteriorate the flow control performance. In the future, these effects should be studied and quantified.

## CRediT authorship contribution statement

**András Szabó:** Conceptualization, Methodology, Software, Investigation, Writing – original draft, Visualisation. **Péter Tamás Nagy:** Methodology, Writing – review & editing. **Gilles De Baets:** Methodology, Writing – review & editing. **Maarten Vanierschot:** Conceptualisation, Writing – review & editing, Funding acquisition. **György Paál:** Conceptualisation, Writing – review & editing, Supervision, Funding acquisition.

## Declaration of competing interest

The authors declare that they have no known competing financial interests or personal relationships that could have appeared to influence the work reported in this paper.

## Data availability

No data was used for the research described in the article.

## Acknowledgements

This research was performed within the framework of NKFI Hungary 142675 project and grant No. CELSA/21/024. András Szabó was supported by the ÚNKP-22-3-II-BME-112 New National Excellence Program of the Ministry for Culture and Innovation from the source of the National Research, Development and Innovation Fund. The work used high performance computing resources, provided by HPC Competence Center of the Governmental Agency for IT grant ID mvgopt01. The authors appreciate the helpful remarks of the anonymous reviewers that substantially improved the paper.

## References

[1] Kachanov YS. Physical mechanisms of laminar-boundary-layer transition. Annu Rev Fluid Mech 1994;26:411–82.
[2] Herbert T. Secondary instability of boundary layers. Annu Rev Fluid Mech 1988;20:487–526.
[3] Gad-el-Hak M. Flow control: Passive, active, and reactive flow management. Cambridge University Press; 2000.
[4] Xu H, Lombard JEW, Sherwin SJ. Influence of localised smooth steps on the instability of a boundary layer. J Fluid Mech 2017;817:138–70.
[5] Luchini P, Trombetta G. Effects of riblets upon flow stability. Appl Sci Res 1995;54:313–21.
[6] Cossu C, Brandt L. On tollmien-schlichting-like waves in streaky boundary layers. Eur J Mech B/Fluids 2004;23:815–33.
[7] Fransson JHM, Talamelli A, Brandt L, Cossu C. Delaying transition to turbulence by a passive mechanism. Phys Rev Lett 2006;96:064501.
[8] Fransson JH. Transition to turbulence delay using a passive flow control strategy. Procedia IUTAM 2015;14:385–93. http://dx.doi.org/10.1016/j.piutam.2015.03.018, URL: https://www.sciencedirect.com/science/article/pii/S2210983815000449. iUTAM_ABCM Symposium on Laminar Turbulent Transition.
[9] Downs RS, Fransson JHM. Tollmien-schlichting wave growth over spanwise-periodic surface patterns. J Fluid Mech 2014;754:39–74.
[10] Pearce HH. Shock-induced separation and its prevention by design and boundary layer control. In: Lachmann GV, editor. Boundary layer and flow control: its principles and application, Vol. 2. Pergamon Press; 1961, p. 1166–344.
[11] Andersson P, Brandt L, Bottaro A, Henningson D. On the breakdown of boundary layer streaks. J Fluid Mech 2001;428:29–60.
[12] Zaki TA. From streaks to spots and on to turbulence: Exploring the dynamics of boundary layer transition. Flow Turbul Combust 2013;91:451–73. http://dx.doi.org/10.1007/s10494-013-9502-8.
[13] Sattarzadeh SS, Fransson JHM. Spanwise boundary layer modulations using finite discrete suction for transition delay. Exp Fluids 2017;58:14.

[14] Sattarzadeh SS, Fransson JHM. Mastering nonlinear flow dynamics for laminar flow control. Phys Rev E 2016;94:021103. http://dx.doi.org/10.1103/PhysRevE.94.021103, URL: https://link.aps.org/doi/10.1103/PhysRevE.94.021103.

[15] Shahinfar S, Sattarzadeh SS, Fransson JHM, Talamelli A. Revival of classical vortex generators now for transition delay. Phys Rev Lett 2012;109:74501.

[16] Fransson JHM, Talamelli A. On the generation of steady streamwise streaks in flat-plate boundary layers. J Fluid Mech 2012;698:211–34.

[17] Shahinfar S, Fransson JHM, Sattarzadeh SS, Talamelli A. Scaling of streamwise boundary layer streaks and their ability to reduce skin-friction drag. J Fluid Mech 2013;733:1–32.

[18] Sattarzadeh SS, Fransson JHM, Talamelli A, Fallenius BEG. Consecutive turbulence transition delay with reinforced passive control. Phys Rev E 2014;89:061001.

[19] Sattarzadeh SS, Fransson JHM. Experimental investigation on the steady and unsteady disturbances in a flat plate boundary layer. Phys Fluids 2014;26:124103.

[20] Downs RS, Fallenius BEG, Fransson JHM, Mårtensson H. Miniature vortex generators for flow control in Falkner–Skan boundary layers. AIAA J 2017;55:352–64.

[21] Shahinfar S, Sattarzadeh SS, Fransson JHM. Passive boundary layer control of oblique disturbances by finite-amplitude streaks. J Fluid Mech 2014;749:1–36.

[22] Sattarzadeh SS, Fransson JHM. On the scaling of streamwise streaks and their efficiency to attenuate tollmien-schlichting waves. Exp Fluids 2015;56:58.

[23] Weingärtner A, Mamidala SB, Fransson JH. Application of miniature vortex generators for boundary layer transition delay. In: AIAA paper 2023-0097. 2023, http://dx.doi.org/10.2514/6.2023-0097, URL: https://arc.aiaa.org/doi/abs/10.2514/6.2023-0097. arXiv:https://arc.aiaa.org/doi/pdf/10.2514/6.2023-0097.

[24] Bagheri S, Hanifi A. The stabilizing effect of streaks on tollmien-schlichting and oblique waves: A parametric study. Phys Fluids 2007;19:78103.

[25] Siconolfi L, Camarri S, Fransson JH. Boundary layer stabilization using free-stream vortices. J Fluid Mech 2014;764:R21–R212.

[26] Brandt L. The lift-up effect: The linear mechanism behind transition and turbulence in shear flows. Eur J Mech B 2014;47:80–96.

[27] Martín JA, Paredes P. Three-dimensional instability analysis of boundary layers perturbed by streamwise vortices. Theor Comput Fluid Dyn 2017;31:505–17.

[28] Martín JA, Paredes P. Transition prediction in incompressible boundary layer with finite-amplitude streaks. Energies 2021;14:2147, 2021, Vol. 14, Page 2147.

[29] Siconolfi L, Camarri S, Fransson JHM. Stability analysis of boundary layers controlled by miniature vortex generators. J Fluid Mech 2015;784:596–618.

[30] Nobis H, Schlatter P, Wadbro E, Berggren M, Henningson D. Topology optimization of roughness elements to delay modal transition in boundary layers. In: Auteri F, Fabre D, Giannetti F, Hanifi A, editors. Progress in flow instability, transition and control, 15th ERCOFTAC SIG33 workshop, ERCOFTAC. 2023, p. 44.

[31] Nobis H, Schlatter P, Wadbro E, Berggren M, Henningson DS. Modal laminar–turbulent transition delay by means of topology optimization of superhydrophobic surfaces. Comput Methods Appl Mech Engrg 2023;403:115721. http://dx.doi.org/10.1016/j.cma.2022.115721, URL: https://www.sciencedirect.com/science/article/pii/S0045782522006764.

[32] Saric W, Ruben Carrillo J, Reibert M. Leading-edge roughness as a transition control mechanism. In: AIAA paper 1998-781. 1998, http://dx.doi.org/10.2514/6.1998-781, URL: https://arc.aiaa.org/doi/abs/10.2514/6.1998-781. arXiv:https://arc.aiaa.org/doi/pdf/10.2514/6.1998-781.

[33] Saric WS, West DE, Tufts MW, Reed HL. Experiments on discrete roughness element technology for swept-wing laminar flow control. AIAA J 2019;57:641–54. http://dx.doi.org/10.2514/1.J056897.

[34] Paredes P, Choudhari MM, Li F. Stabilization of hypersonic boundary layers by linear and nonlinear optimal perturbations. In: AIAA paper 2017-3634. 2017, http://dx.doi.org/10.2514/6.2017-3634, URL: https://arc.aiaa.org/doi/abs/10.2514/6.2017-3634. arXiv:https://arc.aiaa.org/doi/pdf/10.2514/6.2017-3634.

[35] Paredes P, Choudhari MM, Li F. Instability wave–streak interactions in a supersonic boundary layer. J Fluid Mech 2017;831:524–53. http://dx.doi.org/10.1017/jfm.2017.630.

[36] Paredes P, Choudhari MM, Li F. Transition delay via vortex generators in a hypersonic boundary layer at flight conditions. In: AIAA paper 2018-3217. 2018, http://dx.doi.org/10.2514/6.2018-3217, URL: https://arc.aiaa.org/doi/abs/10.2514/6.2018-3217. arXiv:https://arc.aiaa.org/doi/pdf/10.2514/6.2018-3217.

[37] Pederson CC, Choudhari MM, Zhou BY, Paredes P, Diskin B. Shape optimization of vortex generators to control mack mode amplification. In: AIAA aviation 2020 forum 1 part F. 2020.

[38] Klauss CW, Pederson CC, Paredes P, Choudhari MM, Diskin B. Stability analysis of streaks induced by optimized vortex generators. In: AIAA paper 2022-3249. 2022, http://dx.doi.org/10.2514/6.2022-3249, URL: https://arc.aiaa.org/doi/abs/10.2514/6.2022-3249. arXiv:https://arc.aiaa.org/doi/pdf/10.2514/6.2022-3249.

[39] Gould DG. The use of vortex generators to delay boundary layer separation: Theoretical discussion supported by tests on a CF-100 aircraft. Technical report, National Research Council of Canada. Division of Mechanical Engineering. National Aeronautical Establishment; 1956, http://dx.doi.org/10.4224/23001523.

[40] Saric WS, Reed HL, Kerschen EJ. Boundary-layer receptivity to freestream disturbances. Annu Rev Fluid Mech 2002;34:291–319. http://dx.doi.org/10.1146/annurev.fluid.34.082701.161921, arXiv:https://doi.org/10.1146/annurev.fluid.34.082701.161921.

[41] Kerschen EJ. Boundary layer receptivity theory. Appl Mech Rev 1990;43:S152–7. http://dx.doi.org/10.1115/1.3120795, arXiv:https://asmedigitalcollection.asme.org/appliedmechanicsreviews/article-pdf/43/5S/S152/5435839/s152_1.pdf.

[42] Taira K, Brunton SL, Dawson STM, Rowley CW, Colonius T, McKeon BJ, Schmidt OT, Gordeyev S, Theofilis V, Ukeiley LS. Modal analysis of fluid flows: An overview. AIAA J 2017;55:4013–41. http://dx.doi.org/10.2514/1.J056060, arXiv:https://doi.org/10.2514/1.J056060.

[43] Kamal O, Lakebrink MT, Colonius T. Global receptivity analysis: physically realizable input–output analysis. J Fluid Mech 2023;956:R5. http://dx.doi.org/10.1017/jfm.2023.48.

[44] Moulin J, Jolivet P, Marquet O. Augmented lagrangian preconditioner for large-scale hydrodynamic stability analysis. Comput Methods Appl Mech Engrg 2019;351:718–43. http://dx.doi.org/10.1016/j.cma.2019.03.052, URL: https://www.sciencedirect.com/science/article/pii/S0045782519301914.

[45] Towne A, Colonius T. One-way spatial integration of hyperbolic equations. J Comput Phys 2015;300:844–61. http://dx.doi.org/10.1016/j.jcp.2015.08.015, URL: https://www.sciencedirect.com/science/article/pii/S0021999115005343.

[46] Towne A, Rigas G, Kamal O, Pickering E, Colonius T. Efficient global resolvent analysis via the one-way Navier–Stokes equations. J Fluid Mech 2022;948:A9. http://dx.doi.org/10.1017/jfm.2022.647.

[47] Schmid PJ. Nonmodal stability theory. Annu Rev Fluid Mech 2007;39:129–62. http://dx.doi.org/10.1146/annurev.fluid.38.050304.092139, arXiv:https://doi.org/10.1146/annurev.fluid.38.050304.092139.

[48] Garnett R. Bayesian optimization. Cambridge University Press; 2023.

[49] Poulain A, Content C, Sipp D, Rigas G, Garnier E. Broadcast: A high-order compressible cfd toolbox for stability and sensitivity using algorithmic differentiation. Comput Phys Comm 2023;283:108557. http://dx.doi.org/10.1016/j.cpc.2022.108557, URL: https://www.sciencedirect.com/science/article/pii/S0010465522002764.

[50] Bezgin DA, Buhendwa AB, Adams NA. Jax-fluids: A fully-differentiable high-order computational fluid dynamics solver for compressible two-phase flows. Comput Phys Comm 2023;282:108527. http://dx.doi.org/10.1016/j.cpc.2022.108527, URL: https://www.sciencedirect.com/science/article/pii/S0010465522002466.

[51] Jovanović MR. From bypass transition to flow control and data-driven turbulence modeling: An input–output viewpoint. Annu Rev Fluid Mech 2021;53:311–45. http://dx.doi.org/10.1146/annurev-fluid-010719-060244, arXiv:https://doi.org/10.1146/annurev-fluid-010719-060244.

[52] Yeh C-A, Taira K. Resolvent-analysis-based design of airfoil separation control. J Fluid Mech 2019;867:572–610. http://dx.doi.org/10.1017/jfm.2019.163.

[53] Rigas G, Sipp D, Colonius T. Nonlinear input/output analysis: application to boundary layer transition. J Fluid Mech 2021;911:A15. http://dx.doi.org/10.1017/jfm.2020.982.

[54] Sleeman MK, Lakebrink MT, Colonius T. Nonlinear stability of wall-bounded flows using the one-way navier-stokes (owns) equations. In: AIAA paper 2023-3273. 2023, http://dx.doi.org/10.2514/6.2023-3273, URL: https://arc.aiaa.org/doi/abs/10.2514/6.2023-3273. arXiv:https://arc.aiaa.org/doi/pdf/10.2514/6.2023-3273.

[55] Theofilis V. Advances in global linear instability analysis of nonparallel and three-dimensional flows. Prog Aerosp Sci 2003;39:249–315.

[56] Broadhurst MS, Sherwin SJ. The parabolised stability equations for 3d-flows: implementation and numerical stability. Appl Numer Math 2008;58:1017–29. http://dx.doi.org/10.1016/j.apnum.2007.04.016, URL: https://www.sciencedirect.com/science/article/pii/S0168927407000864.

[57] Paredes P, Hanifi A, Theofilis V, Henningson DS. The nonlinear pse-3d concept for transition prediction in flows with a single slowly-varying spatial direction. Procedia IUTAM 2015;14:36–44. http://dx.doi.org/10.1016/j.piutam.2015.03.021, URL: https://www.sciencedirect.com/science/article/pii/S2210983815000474.

[58] Sumariva JAF, Hein SJ. Adaptive harmonic linearized Navier–Stokes equations used for boundary layer instability analysis in the presence of large streamwise gradients. In: AIAA paper 2018-1548. 2018, http://dx.doi.org/10.2514/6.2018-1548, URL: https://arc.aiaa.org/doi/abs/10.2514/6.2018-1548. arXiv:https://arc.aiaa.org/doi/pdf/10.2514/6.2018-1548.

[59] van Ingen J. The en method for transition prediction. historical review of work at tu delft. In: AIAA paper 2008-3830. 2008, http://dx.doi.org/10.2514/6.2008-3830, URL: https://arc.aiaa.org/doi/abs/10.2514/6.2008-3830. arXiv:https://arc.aiaa.org/doi/pdf/10.2514/6.2008-3830.

[60] Huerre P, Monkewitz P A. Local and global instabilities in spatially developing flows. Annual Review of Fluid Mechanics 1990;22(1):473–537. http://dx.doi.org/10.1146/annurev.fl.22.010190.002353.

[61] Schrauf G. Large-scale laminar flow tests evaluated with linear stability theory. J Aircr 2004;41:224–30. http://dx.doi.org/10.2514/1.9280, arXiv:https://doi.org/10.2514/1.9280.

[62] Schrauf GH, von Geyr H. Simplified hybrid laminar flow control for the A320 fin - aerodynamic and system design, first results. 2020, http://dx.doi.org/10.2514/6.2020-1536, URL: https://arc.aiaa.org/doi/abs/10.2514/6.2020-1536. arXiv:https://arc.aiaa.org/doi/pdf/10.2514/6.2020-1536.

[63] Schrauf GH, von Geyr H. Simplified hybrid laminar flow control for the A320 fin. Part 2: Evaluation with the $e^N$-method. 2021, http://dx.doi.org/10.2514/6.2021-1305, URL: https://arc.aiaa.org/doi/abs/10.2514/6.2021-1305. arXiv:https://arc.aiaa.org/doi/pdf/10.2514/6.2021-1305.
[64] Hecht F. New development in freefem++. J Numer Math 2012;20:251–66.
[65] Balay S, Gropp WD, McInnes LC, Smith BF. Efficient management of parallelism in object oriented numerical software libraries. In: Arge E, Bruaset AM, Langtangen HP, editors. Modern Software Tools in Scientific Computing. Boston, MA: Birkhäuser Press; 1997, p. 163–202.
[66] Balay S, Abhyankar S, Adams MF, Benson S, Brown J, Brune P, Buschelman K, Constantinescu E, Dalcin L, Dener A, Eijkhout V, Gropp WD, Hapla V, Isaac T, Jolivet P, Karpeev D, Kaushik D, Knepley MG, Kong F, Kruger S, May DA, McInnes LC, Mills RT, Mitchell L, Munson T, Roman JE, Rupp K, Sanan P, Sarich J, Smith BF, Zampini S, Zhang H, Zhang H, Zhang J. PETSc/TAO users manual. Technical report ANL-21/39 - revision 3.16, Argonne National Laboratory; 2021.
[67] Roman JE, Campos C, Dalcin L, Romero E, Tomas A. SLEPc users manual. Technical report DSIC-II/24/02 - revision 3.18, D. Sistemes Informàtics i Computació, Universitat Politècnica de València; 2022.
[68] Martín JA, Martel C. Nonlinear streak computation using boundary region equations. Fluid Dyn Res 2012;44:045503. http://dx.doi.org/10.1088/0169-5983/44/4/045503.
[69] Paredes P. Advances in global instability computations: From incompressible to hypersonic flow. (Ph.D. thesis), Universidad Politécnica de Madrid; 2014.
[70] Bridges TJ, Morris PJ. Differential eigenvalue problems in which the parameter appears nonlinearly. J Comput Phys 1984;55:437–60. http://dx.doi.org/10.1016/0021-9991(84)90032-9.
[71] Herbert T. Parabolized stability equations. In: Agard-R-793: Special course on progress in transition modeling. 1994.
[72] Camarri S, Fransson JHM, Talamelli A. Numerical investigation of the afrodite transition control strategy. In: Talamelli A, Oberlack M, Peinke J, editors. Progress in turbulence V. Cham: Springer International Publishing; 2014, p. 65–9.
[73] ANSYS 21 R2 CFX theory guide. ANSYS Inc.; 2021.
[74] Geuzaine C, Remacle J-F. Gmsh: A 3-d finite element mesh generator with built-in pre- and post-processing facilities. Internat J Numer Methods Engrg 2009;79:1309–31. http://dx.doi.org/10.1002/nme.2579, URL: https://onlinelibrary.wiley.com/doi/abs/10.1002/nme.2579. arXiv:https://onlinelibrary.wiley.com/doi/pdf/10.1002/nme.2579.
[75] Hecht F. BAMG: Bidimensional anisotropic mesh generator. INRIA; 1998.
[76] Amestoy PR, Duff IS, L'Excellent J-Y, Koster J. A fully asynchronous multifrontal solver using distributed dynamic scheduling. SIAM J Matrix Anal Appl 2001;23:15–41. http://dx.doi.org/10.1137/S0895479899358194, arXiv:https://doi.org/10.1137/S0895479899358194.
[77] Amestoy PR, Buttari A, L'Excellent J-Y, Mary T. Performance and scalability of the block low-rank multifrontal factorization on multicore architectures. ACM Trans Math Software 2019;45. http://dx.doi.org/10.1145/3242094.
[78] Campos C, Roman JE. Parallel Krylov solvers for the polynomial eigenvalue problem in SLEPc. SIAM J Sci Comput 2016;38:S385–411.
[79] Andersson P, Berggren M, Henningson DS. Optimal disturbances and bypass transition in boundary layers. Phys Fluids 1999;11:134–50. http://dx.doi.org/10.1063/1.869908, arXiv:https://doi.org/10.1063/1.869908.
[80] De Vincentiis L, Henningson DS, Hanifi A. Transition in an infinite swept-wing boundary layer subject to surface roughness and free-stream turbulence. J Fluid Mech 2022;931:A24. http://dx.doi.org/10.1017/jfm.2021.962.
[81] Ribeiro JHM, Yeh C-A, Taira K. Randomized resolvent analysis. Phys Rev Fluids 2020;5:33902.
[82] Trefethen LN, Embree M. Spectra and pseudospectra. Princeton: Princeton University Press; 2005, http://dx.doi.org/10.1515/9780691213101.
[83] Schmid P, Henningson DS. Stability and transition in shear flows, Vol. 142. 2001, http://dx.doi.org/10.1007/978-1-4613-0185-1.
[84] Brandt L, Sipp D, Pralits JO, Marquet O. Effect of base-flow variation in noise amplifiers: The flat-plate boundary layer. J Fluid Mech 2011;687:503–28.